JACS
JOURNAL OF THE AMERICAN CHEMICAL SOCIETY

Article

pubs.acs.org/JACS

Processing Pathway Dependence of Amorphous Silica Nanoparticle Toxicity: Colloidal vs Pyrolytic

Haiyuan Zhang,[†] Darren R. Dunphy,[‡] Xingmao Jiang,[‡,§] Huan Meng,[∥] Bingbing Sun,[†] Derrick Tarn,[⊥] Min Xue,[⊥] Xiang Wang,[†] Sijie Lin,[†] Zhaoxia Ji,[†] Ruibin Li,[†] Fred L. Garcia,[‡] Jing Yang,[□] Martin L. Kirk,[□] Tian Xia,[∥] Jeffrey I. Zink,[⊥] Andre Nel,[†,∥] and C. Jeffrey Brinker*[,‡,●,¶]

[†]California NanoSystems Institute, University of California, 570 Westwood Plaza, Los Angeles, California 90095, United States

[‡]Department of Chemical and Nuclear Engineering, University of New Mexico, 1 University of New Mexico MSC01 1120, Albuquerque, New Mexico 87131, United States

[§]Jiangsu Key Laboratories of Advanced Catalytic Materials and Technology and Fine Petrochemical Engineering, Changzhou University, Changzhou, 213164, PR China

[∥]Division of NanoMedicine, Department of Medicine, University of California, 10833 Le Conte Ave, Los Angeles, California 90095, United States

[⊥]Department of Chemistry and Biochemistry, University of California, 607 Charles E. Young Drive East, Los Angeles, California 90095, United States

[□]Department of Chemistry and Chemical Biology, University of New Mexico, 1 University of New Mexico MSC03 2060, Albuquerque, New Mexico 87131, United States

[●]Department of Molecular Genetics and Microbiology, University of New Mexico, 1 University of New Mexico MSC 08-4660, Albuquerque, New Mexico 87131, United States

[¶]Self-Assembled Materials Department, Sandia National Laboratories, PO Box 5800 MS1349, Albuquerque, New Mexico 87185, United States

Supporting Information

ABSTRACT: We have developed structure/toxicity relationships for amorphous silica nanoparticles (NPs) synthesized through low-temperature colloidal (e.g., Stöber silica) or high-temperature pyrolysis (e.g., fumed silica) routes. Through combined spectroscopic and physical analyses, we have determined the state of aggregation, hydroxyl concentration, relative proportion of strained and unstrained siloxane rings, and potential to generate hydroxyl radicals for Stöber and fumed silica NPs with comparable primary particle sizes (16 nm in diameter). On the basis of erythrocyte hemolytic assays and assessment of the viability and ATP levels in epithelial and macrophage cells, we discovered for fumed silica an important toxicity relationship to postsynthesis thermal annealing or environmental exposure, whereas colloidal silicas were essentially nontoxic under identical treatment conditions. Specifically, we find for fumed silica a positive correlation of toxicity with hydroxyl concentration and its potential to generate reactive oxygen species (ROS) and cause red blood cell hemolysis. We propose fumed silica toxicity stems from its intrinsic population of strained three-membered rings (3MRs) along with its chainlike aggregation and hydroxyl content. Hydrogen-bonding and electrostatic interactions of the silanol surfaces of fumed silica aggregates with the extracellular plasma membrane cause membrane perturbations sensed by the Nalp3 inflammasome, whose subsequent activation leads to secretion of the cytokine IL-1β. Hydroxyl radicals generated by the strained 3MRs in fumed silica, but largely absent in colloidal silicas, may contribute to the inflammasome activation. Formation of colloidal silica into aggregates mimicking those of fumed silica had no effect on cell viability or hemolysis. This study emphasizes that not all amorphous silicas are created equal and that the unusual toxicity of fumed silica compared to that of colloidal silica derives from its framework and surface chemistry along with its fused chainlike morphology established by high-temperature synthesis (>1300 °C) and rapid thermal quenching.

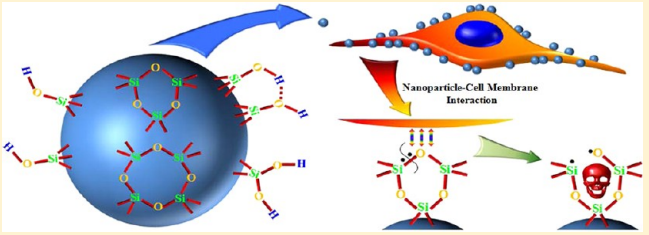

1. INTRODUCTION

Silicon dioxide *silica* is the most abundant mineral on earth—predominantly in the form of alpha-crystalline quartz.[1] Man-made silicas, however, tend to be amorphous and often used as nanostructured powders in applications such as fillers to control rheological and mechanical behaviors, catalysts, and desiccants.[2] Amorphous silica nanoparticles are prepared by two main

Received: May 21, 2012
Published: August 28, 2012

   dx.doi.org/10.1021/ja304907c | J. Am. Chem. Soc. 2012, 134, 15790−15804

routes, high-temperature flame pyrolysis to form so-called *fumed or pyrolytic silica* (by the net reaction $SiCl_4 + 2H_2O \rightarrow SiO_2 + 4HCl$) conducted at temperatures ranging from 1200 to 1400 °C followed by rapid thermal quenching[3] or by molecular condensation of silanol groups (≡Si−OH + HO−Si≡ ⇔ ≡Si−O−Si≡) in aqueous solution or under hydrothermal conditions to form so-called *precipitated, colloidal, or mesoporous silicas.*[4,5] Both fumed silica and colloidal silica are produced in tonnage quantities—the worldwide production of amorphous silica nanoparticles was estimated to be 1.3 t per annum in 2000[2]—making amorphous silica NPs arguably the most abundant synthetic nanoparticles on earth. On the basis of the abundance and potential exposure to amorphous silica NPs, establishing structure activity relationships (SARs) is important for understanding the pathways of silicosis and silica-related diseases and addressing the provocative question of whether crystallinity is the prerequisite feature that makes a silica dust toxic.[6] Establishing SARs for amorphous silica is problematic, however. Whereas crystalline silica is well-defined structurally, amorphous silicas lack long-range order, and due to a flat energy landscape, their structures are strongly dependent on kinetic and environmental factors.[7] For amorphous silica NPs these factors are manifested principally as differences in the siloxane framework architecture, which consists of combinations of closed siloxane rings (Scheme 1),[8] along with the

Scheme 1. Schematic Depicting the Ring Structure of Amorphous Silica and the Amorphous Silica Surface after Equilibration with Hydroxyl Groups

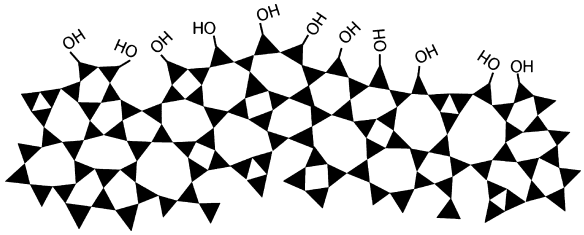

concentration, pattern, and extent of hydrogen bonding of silanol groups (≡Si−OH) that terminate the siloxane rings at the silica NP surface (Scheme 2).[4,5] Due to their high surface area, it is also anticipated that silica NPs could contain relatively high concentrations of surface-associated radicals (Scheme 3).[9,10]

Scheme 2. Types of Silanol Groups That Can Exist on the Amorphous Silica Surface

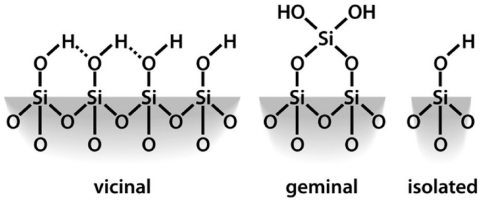

In spite of numerous studies of the toxicity of amorphous and crystalline silicas,[11−14] the mechanism(s) by which silica exposure leads to silicosis and chronic inflammation remains unclear.[11,15,16] Amorphous silica is 'generally considered safe' by the U.S. Federal Drug Administration, and amorphous silica nanoparticles are often used as 'negative controls' in toxicity studies of nanocrystalline quartz.[6,17] However, due to the

Scheme 3. Radicals That Can Exist on the Amorphous Silica Surface

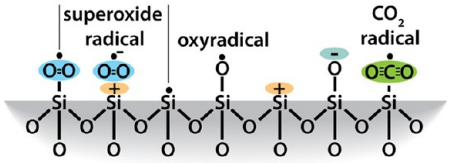

diversity of possible amorphous silica nanoparticle structures, their toxicological behaviors are less well understood and are expected to be more variable than for crystalline materials. Correspondingly, there are numerous reports documenting the toxicity of amorphous silica nanoparticles and their potential to cause red blood cell lysis.[18−23] In many cases noncrystalline silicas are referred to simply as amorphous silica or vitreous silica,[6,17,22,24] without regard to thermal and chemical processing conditions or levels of environmental exposure, which alter framework and surface chemistry[4,25] and thus colloidal, biomolecular, and toxicological behaviors.[26,27] Because the surface chemistry, size, and shape are all implicated in nanoparticle toxicity,[27] detailed characterization and understanding of the physicochemical properties of silica nanoparticles and the systematic variation of these properties is needed to develop structure/toxicity relationships. The purpose of this paper is to comprehensively characterize the physicochemical and toxicological properties of the two principal classes of amorphous silica nanoparticles, fumed silica and colloidal silica (Stöber silica), prepared with nearly identical primary particle sizes and subjected to different conditions of environmental exposure. On the basis of the similar coverages of surface silanols (≡Si−OH, which are implicated as effectors of silica toxicity)[22,28] measured for a wide range of amorphous silica materials,[29] it might be expected that amorphous silica NPs would in turn show comparable toxicities when compared on a surface area normalized basis.[27] However, we show that silica nanoparticles of comparable primary particle size and hydroxyl coverage can have distinctly different toxicity profiles. This study provides novel insight into understanding the hazard potential of amorphous silica and suggests design principles for biocompatible amorphous silica nanoparticles of potential use for therapeutic and diagnostic applications.

2. EXPERIMENTAL SECTION

2.1. Materials and Methods. Fumed silica, with an approximate 16-nm diameter primary particle size (AEROSIL, Evonik Degussa GmbH), was purchased from Sigma Aldrich and was used 'as received', or following heating of the material in air to 200−800 °C for 6 h or after heating to 800 °C for 6 h followed by reflux in DI water for 24 h. Colloidal silica NPs were synthesized by base-catalyzed hydrolysis of TEOS via a modification of the well-known Stöber process (see Supporting Information for details).[30] Stöber silica nanoparticles were used 'as prepared' following drying and redispersion, or after heating in air to 200−800 °C for 6 h or after heating to 800 °C for 6 h followed by reflux in DI water for 24 h. Aggregates of Stöber silica NPs were synthesized by electrostatic destabilization of the parental colloidal sols by addition of 0.5 mL of 1.0 M NaCl (see Supporting Information [SI] for details).

TEM was performed on samples dispensed from alcohol onto holey carbon substrates using a JEOL 2010 microscope operated at 200 keV. Confocal fluorescent microscopy images were acquired using a Leica Confocal 1P/FCS microscope in the UCLA/CNSI Advanced Light Microscopy/Spectroscopy Shared Facility. Silica was fluorescently

dx.doi.org/10.1021/ja304907c | J. Am. Chem. Soc. 2012, 134, 15790−15804

labeled by conjugation of amino-propyl-modified silica NPs with FITC (see SI for details). Surface area was determined by the BET method from N_2 sorption isotherms acquired using a Micromeritics ASAP 2010 sorption instrument following outgassing under vacuum for 12 h at 120 °C. Zeta potential and dynamic light scattering (DLS) data were obtained using a Malvern Nanosizer ZS for silica NPs dispersed with BSA at a concentration of 2 mg/mL. Weight loss due to dehydration and dehydroxylation was determined by TGA (TA Instruments, model STD 2960) and used to derive a measure of the OH concentration independent of the FTIR results. Near and mid-infrared spectra were obtained on free-standing pressed pellets using a Nicolet 6700 FTIR equipped with either an InGaAs or DTGS detector, respectively. Raman spectra were recorded on free-standing pressed pellets using a DXR SmartRaman system at a wavelength of 785 nm. Free radical release was determined by electron paramagnetic (EPR) spectroscopy using the spin trap technique performed according to literature procedures developed for silica materials.[31,32] Room temperature X-band (9.4 GHz) spectra were recorded with a Bruker ESP 300 electron paramagnetic resonance (EPR) spectrometer equipped with a Bruker ER041XG microwave bridge. 5,5-Dimethyl-pirroline-*N*-oxide (DMPO) was used as the spin-trapping molecule. Five weight percent samples were dispersed in DI water with 25 mM DMPO and 200 mM H_2O_2, and spectra were recorded after a 15-min equilibration time at room temperature. Neutron scattering experiments were performed at the Lujan Neutron Scattering Center (LANSCE) LQD beamline on samples dispersed in D_2O. Total and isolated hydroxyl concentrations were determined by integration of the near-IR band centered at 4500 cm^{-1} and mid-IR band centered at 3750 cm^{-1} and applying Beers law with molar absorptivity coefficients of 0.16 and 4 $\mu M/cm^{-1}$,[33] respectively. Hydrogen-bonded silanol concentrations were determined by difference.

2.2. Silica Nanoparticle Dispersion in Cell Culture Media.[34] Silica nanoparticle stock solutions (5 mg/mL) were prepared by dispersing the dry particles in deionized water through probe sonication (3 W). The stock solution was used to remove 40 μL aliquots which were mixed with an equal volume of 4% bovine serum albumin (BSA) (Fraction-V, Gemini Bioproducts, United States) and equilibrated for 1 h at room temperature. Cell culture media (920 μL) were added to the BSA-coated nanoparticle suspensions, which were further stabilized by the addition of 2 mg/mL BSA. The nanoparticle suspensions were sonicated (3 W) for 15 s prior to conducting cellular studies.

2.3. Cell Culture. Human bronchial epithelial cell lines (BEAS-2B), mouse macrophage cell lines (RAW 264.7) and human acute monocytic leukemia cells (THP-1) were cultured in vented T-75 cm^2 flasks (Corning, Fisher Scientific, Pittsburgh, PA) at 37 °C in a humidified 5% CO_2 atmosphere, and passaged at 70−80% confluency every 2−4 days. BEAS-2B cells were cultured in bronchial epithelial basal medium (BEBM) (Lonza, Walkersville, MD, United States), supplemented with growth factors from the SingleQuot kit (Lonza) to make BEGM. RAW 264.7 cells were cultured in DMEM medium containing 10% fetal calf serum (FCS), 100 U/mL penicillin, 100 $\mu g \cdot mL^{-1}$ streptomycin, and 2 mM L-glutamine. THP-1 cells were cultured in RPMI 1640 medium containing 10% fetal calf serum (FCS), 100 U/mL penicillin, 100 $\mu g \cdot mL^{-1}$ streptomycin, and 2 mM L-glutamine.

2.4. Cytotoxicity Assessment by Single Parameter Assays.[35] Cell death, cell viability, and intracellular ATP levels were determined by LDH, MTS, and ATP assays, which were carried out with CytoTox 96 (Promega Corporation, Madison, WI, United States), CellTiter 96 AQueous (Promega Corporation) and ATPliteTM firstep (Perkin-Elmer, Boston, MA, United States) assay kits, respectively.[35] Ten thousand cells in 100 μL of medium were plated in each well of a 96-multiwell black plate (Costar, Corning, NY, United States) for overnight growth. The medium was removed, and cells were treated for 24 h with 100 μL of a series of nanoparticle suspensions to yield final concentrations of 0.4, 0.8, 1.6, 3.2, 6.3, 12.5, 25, 50, 100, and 200 $\mu g \cdot mL^{-1}$. For the LDH assay, supernatants were transferred to a new 96-multiwell plate and centrifuged at 2000*g* for 10 min in an Eppendorf 5430 microcentrifuge with microplate rotor to spin down the cell debris and nanoparticles. Fifty microliters of the supernatant was removed from each well and transferred into a new 96-well plate and mixed with 50 μL of reconstituted substrate solution for 30 min at room temperature in the dark. The reaction was terminated by the addition of 50 μL stop solution. Cells treated with the Lysis Solution (provided by manufacturer) for 45 min were used as the positive control. Three independent experiments and three replicates for each experiment were performed. The absorbance of formazan was read at 490 nm on a SpectraMax M5 microplate spectrophotometer (Molecular Devices, Sunnyvale, CA, United States). For the MTS assay, the cell culture medium was removed, and following washing of the plates three times with PBS, each well received 100 μL of culture medium containing 16.7% of MTS stock solution for an hour at 37 °C in a humidified 5% CO_2 incubator. The supernatants were transferred to a new 96-multiwell plate and centrifuged at 2000*g* for 10 min in an Eppendorf 5430 microcentrifuge with microplate rotor to spin down the cell debris and nanoparticles. Eighty microliters of the supernatant was removed from each well and transferred into a new 96-well plate. The absorbance of formed formazan was read at 490 nm on a SpectraMax M5 microplate spectrophotometer. To perform the ATP assay, cells used for performing the MTS assay were washed three times with PBS and incubated with 100 μL of reconstituted ATPlite firstep reagent for 10 min. The luminescence intensity was recorded on a SpectraMax M5 microplate spectrophotometer.

2.5. Use of a Multiparametric Assay to Compare the Cytotoxicity of Silica Nanoparticles. The rationale for using this assay, which quantitatively assesses cellular oxidative stress parameters, has been previously described.[34] Five thousand cells in 50 μL of tissue culture medium were plated into each well of a 384-multiwell plate (Greiner Bio-One, Monroe, NC, United States), followed by overnight growth at 37 °C in a humidified 5% CO_2 incubator. The medium in each well was aspirated, and 25 μL of a nanoparticle dilution series was added to quadruplicate wells to deliver a dose range of 0.4, 0.8, 1.6, 3.2, 6.3, 12.5, 25, 100, and 200 $\mu g \cdot mL^{-1}$.[35] This work was carried out in the Molecular Shared Screening Resource laboratory in the California NanoSystems Institute, where cellular seeding of the plates, preparation of the nanoparticle working solutions, and their addition to the tissue culture plates are carried out with automated liquid handling devices including a Multidrop (Thermo-Fischer, Waltham, MA, United States), Precision 2000 (Biotek Instruments, Winooski, VT, United States) and Hydra 96 (Robbins Scientific, Golden Valley, MN, United States).[34] Three cocktails of fluorescent dye mixtures were prepared by mixing dyes with compatible wavelengths in BEGM or complete DMEM.[35] The first cocktail contained Hoechst 33342 (1 μM), Fluo-4 (5 μM), and propidium iodide (5 μM); the second cocktail contained Hoechst 33342 (1 μM), DCF (5 μM), and MitoSox Red (5 μM), and the third, Hoechst 33342 (1 μM) and JC-1 (5 μM). The utility of these dyes, their excitation/emission wavelengths, and response profiling have been described previously.[35] Each well received 2.5 μL of one of the dye mixtures for 30 min, with the plates being kept under dark cell culture conditions. Epifluorescence readings were obtained hourly for the first 6 h and again at the 24-h mark, using an Image-Xpress Micro high content screening system (Molecular Devices, Sunnyvale, CA, United States) equipped with a laser autofocus. DAPI, FITC, and TRITC filter/dichroic combinations were used to image Hoechst 33342 (blue), Fluo-4/DCF/JC-1 (green), and PI/MitoSox Red (red), respectively. Images were processed using MetaXpress software (Molecular Devices, Sunnyvale, CA, United States) at 10 × magnification. The total number of nuclei was counted in the Hoechst/DAPI channel using the following settings: The minimum width was 3 μm (about 3 pixels), the approximate maximum width was 10 μm (about 7 pixels) and the threshold intensity was 100 gray levels above background. For the FITC and TRITC channels the approximate minimum width was 5 μm (about 6 pixels) and the approximate maximum width was 30 μm (about 22 pixels). The thresholds were set at 250 and 500 gray levels, respectively, above background. The percentage of cells positive for each response parameter was calculated using MetaXpress software on the basis of the total number of Hoechst-positive cells showing increased

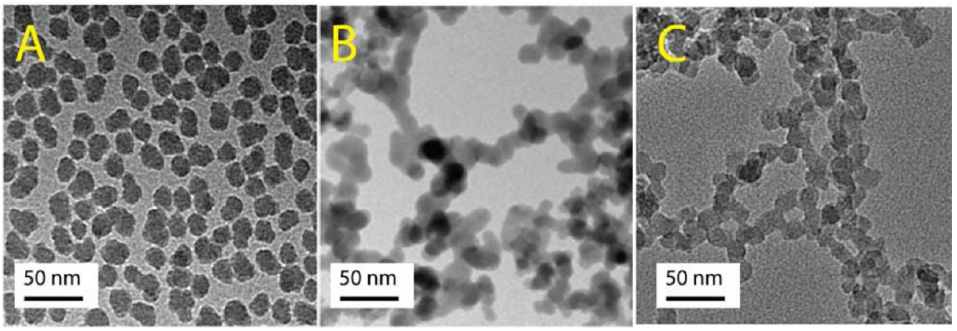

Figure 1. TEM images. (A) Stöber silica colloidal silica NPs; (B) "as-received" fumed silica NP aggregates; (C) "as-prepared" Stöber silica NPs aggregated by 0.1 M NaOH and aged at pH 2 for 12 h at room temperature.

fluorescence intensity above a defined threshold for each particular dye.

The HTS toxicity data were first normalized via strictly standard mean difference (SSMD) to quantify the cell responses induced by the nanoparticles.[36−38] SSMD measures the magnitude of the differences between each set of quadruplicate measurements and the control population (cell population that were not exposed to ENMs) standardized by their variances with the following definition,

$$\mathrm{SSMD} = (\mu_{\mathrm{sample}} - \mu_{\mathrm{control}})/\sqrt{\sigma^2_{\mathrm{sample}} - \sigma^2_{\mathrm{control}}}$$

where μ and σ respectively denote the mean and standard deviation of the sample quadruplicate or the control population (identified by the subscripts). |SSMD| $\geq$ 3 indicates a significant difference between the nanoparticle-induced cell response to control (given that the mean difference is normally distributed, a |SSMD| of 3 indicates the probability that the sample population is different from the control population is >99%).

2.6. Hemolysis Assay.[22] Heparinized mouse blood was washed to remove the serum, following which the red blood cells (RBC) were washed five times with sterile isotonic PBS solution. The RBC were diluted 10× their initial volume in sterile isotonic PBS solution. 300 μL of the diluted RBC suspension was mixed with 1200 μL of PBS as a negative control or with 1200 μL PBS containing 0.025% Triton X-100 as a positive hemolysis control. Silica nanoparticles, suspended in 1200 μL PBS, were added to the diluted RBC suspension at 25 to 100 μg·mL^{-1}. The mixtures were vortexed and incubated for 2 h at room temperature. The samples were centrifuged and the absorbance of the supernatants measured at 541 nm in a SpectraMax M5 microplate spectrophotometer. The percent hemolysis in each sample was calculated by dividing the difference in absorption between the sample and the negative control by the difference in absorption between the positive and negative controls, then multiplying this ratio by 100 to obtain % hemolysis.

2.7. IL-1β Quantification by ELISA. Twenty thousand THP-1 cells in 100 μL of medium containing 1 μg·mL^{-1} of phorbol-12-myristate-13-acetate (PMA) were plated in each well of a 96-multiwell black plate (Costar, Corning, NY, United States) for overnight growth. The medium was removed and cells treated for 24 h with 100 μL of a series of nanoparticle suspensions to yield final concentrations of 0.4, 0.8, 1.6, 3.2, 6.3, 12.5, 25, 50, 100, and 200 μg·mL^{-1}. The 96-multiwell black plate was centrifuged at 2000*g* for 10 min in an Eppendorf 5430 microcentrifuge with microplate rotor to spin down the cell debris and nanoparticles. Fifty microliters of the supernatant was removed from each well for measurement of IL-1β activity by using an OptEIA (BD Biosciences, CA, United States) ELISA kit according to the manufacturer's instructions.[39] Briefly, a 96-well plate was coated with 50 μL of monoclonal anti-IL-1β for 2 h. After removal of the monoclonal anti-IL-1β solution, the supplied standard growth factor dilution series or 50 μL of above supernatants was pipetted into the monoclonal anti-IL-1β precoated wells for antigen capture. After 2 h, the unbound growth factor was removed, and each well in the plate was washed with buffer (provided by the manufacturer) five times, and an enzyme-linked anti-IL-1β polyclonal was added. Following washing to remove unbound secondary antibody, a substrate solution was added at 1:250 dilution for 30 min to allow color development. After termination of the reaction, the colorometric intensity was measured at 450 nm in a plate reader (SpectroMax M5, Molecular Devices Corp., Sunnyvale, CA, United States).

2.8. Cathepsin B Release from Lysosome Assessed by Magic Red. Cathepsin B release from lysosomes was evaluated by confocal microscopy using a Magic Red Cathepsin B assay kit (Immunochemistry Technologies, LLC., Bloomington, MN, USA) according to the manufacturer's instructions.[40] 1 × 10^5 THP-1 cells in 400 μL of RPMI medium containing 1 μg·mL^{-1} of PMA were plated in each well of an 8-well chamber slide. After overnight incubation at 37 °C in a humidified 5% CO_2 atmosphere, dispersed nanoparticles were added at a dose of 25 μg·mL^{-1} for 5 h. After treatment, cells were washed three times with PBS and further stained with Magic Red working solution for 1 h at 37 °C in a humidified 5% CO_2 atmosphere. After staining, cells were washed three times with PBS and fixed in 400 μL of PBS containing 4% paraformaldehyde for 1 h. Cell nuclei were stained with 5 μg·mL^{-1} Hoechst 33342, while cell membranes were stained with 5 μg·mL^{-1} Alexa Fluor 488-conjugated wheat germ agglutinin (WGA) for 30 min. Cells were washed with PBS three times and visualized under a confocal microscope (Leica Confocal SP2 1P/FCS) in the UCLA/CNSI Advanced Light Microscopy/Spectroscopy Shared Facility. High-magnification images were obtained with a 63× objective. Optical sections were averaged 4 times to reduce noise. Images were processed using Leica Confocal Software.

2.9. Confocal Fluorescence Microscopy to Study Cellular Association and Localization of FITC-Labeled Fumed or Stöber Silica Nanoparticles. The association and cellular distribution of FITC-labeled fumed or Stöber silica nanoparticles with BEAS-2B or THP-1 cells was assessed by confocal microscopy. One ×10^5 cells in 400 μL of medium (BEGM or RPMI containing 1 μg·mL^{-1} PMA) were plated in each well of an 8-well chamber slide. After overnight growth at 37 °C in a humidified 5% CO_2 atmosphere, the FITC-labeled particles were added at a dose of 25 μg·mL^{-1} for 5 h. After treatment, cells were washed three times with PBS and fixed in 400 μL of PBS containing 4% paraformaldehyde for 1 h. Cell nuclei were stained with 5 μg·mL^{-1} Hoechst 33342, while cell membranes were stained with 5 μg·mL^{-1} Alexa Fluor 594-conjugated WGA for 30 min. Cells were washed with PBS three times and visualized under a confocal microscope (Leica Confocal SP2 1P/FCS) in the UCLA/CNSI Advanced Light Microscopy/Spectroscopy Shared Facility. High-magnification images were obtained with a 63× objective. Optical sections were averaged four times to reduce noise. Images were processed using Leica Confocal Software.

2.10. Cellular Transmission Electron Microscopy. Ten milliliters of 1 × 10^5 BEAS-2B cells in BEGM medium, containing 2 mg/mL BSA, were seeded in a 10-cm Petri dish for overnight growth at 37 °C in a humidified 5% CO_2 atmosphere. Cells were treated with 25 μg·mL^{-1} fumed silica or Stöber silica nanoparticles for 5 h. After treatment, cells were gently washed three times with PBS and fixed in 5 mL of 2% glutaraldehyde in 0.1 M phosphate-buffered saline (PBS) for 2 h. Cells were scratched from the plate bottom and collected for postfixation in 1% OsO_4 in PBS. After 1 h fixation, cells were

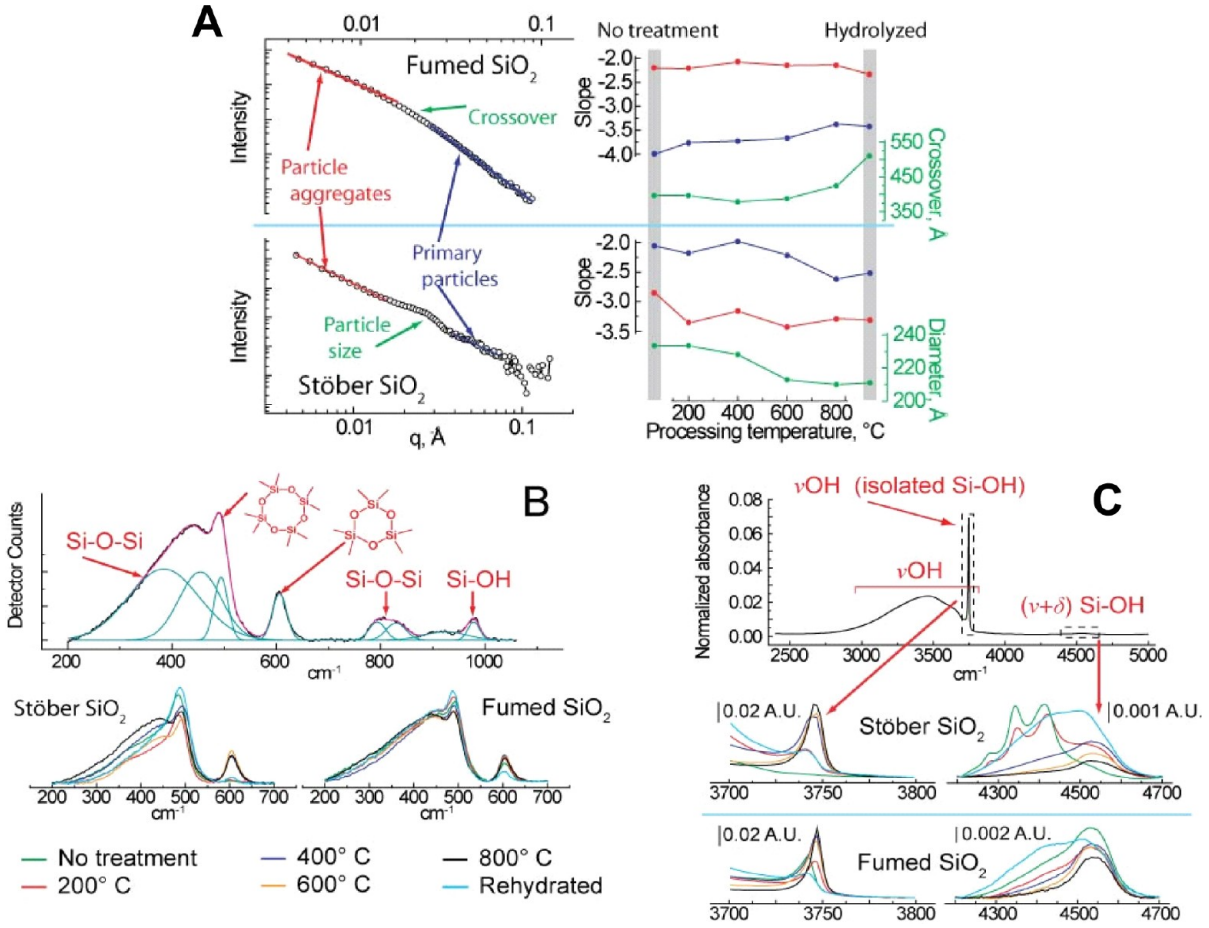

Figure 2. Physical and spectroscopic characterization of ~16 nm amorphous fumed and Stöber silica nanoparticles. (A) Small-angle neutron scattering (SANS) analysis of fumed and Stöber silica structure as a function of processing, with the slope of the scattering curve at low and high **q** indicative of aggregate and individual particle morphology, respectively. For fumed silica, the crossover is the point of transition between these two regions. Instead of a crossover, Stöber silica exhibits a scattering peak indicative of monodisperse nanoparticles, with the particle diameter indicated by the **q** position of this feature. (B) Raman spectroscopy of silica samples used to examine the relative concentration of four- and three-membered ring structures. The top panel illustrates a sample peak fit of a typical spectrum, while the bottom panels show data for fumed and Stöber silica as a function of processing, normalized using the peak area of the Si−O−Si band at ~800 cm^{-1}. (C) FTIR analysis of silanol concentration in fumed and Stöber silica using vibrational bands at ~3745 cm^{-1} (non-hydrogen bonded silanols only) and 4500 cm^{-1} (total silanol population), including representative spectra obtained as a function of material processing (legend at bottom of plot).

dehydrated in a graded ethanol series, treated with propylene oxide, and embedded in Epon. Thick sections (50−70 nm) were sliced using a Reichert-Jung Ultracut E ultramicrotome and captured on Formvar-coated copper grids. The sections were stained with uranyl acetate and Reynolds lead citrate and examined on a JEOL 100 CX transmission electron microscope at 80 kV in the UCLA BRI Electron Microscopy Core.

2.11. Statistical Analysis. All data were expressed as mean ± SD. All values were obtained from at least three independent experiments. Statistical significance was evaluated using two-tailed heteroscedastic Student's *t*-tests according to the TTEST function in Microsoft Excel. The significant difference between groups was considered statistically significant when the *p*-value was lower than 0.05.

3. RESULTS

3.1. Physicochemical Characterization. The key physicochemical properties of the fumed and colloidal (Stöber) silica NPs are summarized in Figures 1-3 and in SI Table S1, in which we make comparisons to amorphous mesoporous silica nanoparticles, LUDOX (a commercial colloidal silica NP), crystalline Min-U-Sil (alpha-quartz), and silicalite (the pure silica zeolite) used as controls and reference materials. As shown by the TEM micrographs in Figure 1, both the fumed and colloidal silica NPs are characterized by a ~16-nm primary particle size. For "as-prepared" colloidal particles, the primary particles are shown to be nonaggregated after drying from alcohol (Figure 1A), whereas, "as-received" fumed silica nanoparticles are composed of ramified chainlike aggregates (Figure 1B). Figure 1C shows that chainlike aggregates with morphologies comparable to those of fumed silica can be obtained through electrostatic destabilization and aging of the parent Stöber colloidal NPs. DLS (SI Table S1) and neutron scattering results (Figure 2A) show that aqueous dispersions of NPs are aggregated to differing extents depending on the processing method, heat treatment, and addition of BSA or media used as dispersion agents. The power law neutron scattering exponents at low scattering wave vector **q** provide statistical information regarding the morphology of the aggregates.[41] Exponents of ~−2.1 observed for fumed silica provide evidence for fractal aggregates (fractal dimension d_f = 2.1) formed by kinetically limited aggregation during aerosol processing[42] (as apparent also in TEM-Figure 1B). Fractal aggregates have been identified by related small-angle X-ray and light scattering for other commercial fumed silicas (e.g., d_f = 1.9

dx.doi.org/10.1021/ja304907c | J. Am. Chem. Soc. 2012, 134, 15790−15804

for Cab-O-Sil),[42] and occur in general for nanoparticles synthesized by flame pyrolysis.[3,43] Exponents more negative than −3 observed for Stöber silica provide evidence of more compact fractally rough aggregates that form during dispersion of the primary particles in solution. High **q** exponents give information regarding surface roughness of the primary particles, where −4 observed for fumed silica indicates a smooth particle/water interface as expected from its high-temperature synthesis, while exponents decreasing from −2 to −2.5 observed for colloidal silica are evidence of rough primary particle surfaces that become progressively smooth with heating.[44]

Figure 2B compares the Raman spectra of fumed and Stöber silica for different treatments normalized to the ∼800 cm^{-1} band attributed to the total silica content of the sample. Most striking is the comparison between the "as-received" fumed silica and "as-prepared" Stöber silica NPs, where for fumed silica we observe prominent narrow bands at ∼600 cm^{-1} and 490 cm^{-1} attributed to three- and four-membered siloxane rings, respectively.[25] There is also a broader band centered at ∼450 cm^{-1} attributed to five-membered and larger siloxane rings. The "as-prepared" Stöber silica NPs have a prominent 490 cm^{-1} band but no 600 cm^{-1} band and a rather weakly developed 450 cm^{-1} band. These differences reflect distinctly different synthesis conditions, where for fumed silica, thermal quenching freezes in a high-temperature silica structure with an intrinsic population of both strained 3MRs (observed also for Aerosil fumed silica synthesized with 7, 14, or 40-nm primary particle size)[45] as well as larger unstrained rings. Stöber silica evolves in solution via continued condensation reactions involving principally unstrained four-membered and larger rings.[5] The absence of 3MRs is characteristic of other solution-derived silica nanoparticles including mesoporous silica[46] and LUDOX (see SI Figure S1)[25] as well as silica gels.[4] Figure 2C compares the corresponding near- and mid-IR spectra of fumed and Stöber silica NPs for different treatment conditions. These spectra are composed of a broad combination band centered at 4500 cm^{-1}, attributed to the total (hydrogen-bonded and isolated) hydroxyl concentration, and broad and narrow peaks centered at 3460 cm^{-1} and 3750 cm^{-1}, attributed to hydrogen-bonded vicinal and isolated silanols, respectively. Comparison of the "as-prepared" NPs indicates that Stöber silica NPs, which are synthesized under water equilibration at low temperature, have a higher total silanol content ∼4.5 OH/nm^2, which corresponds closely to a fully hydroxylated amorphous silica surface,[29,47] but no isolated silanols; i.e., the surface is composed of hydrogen-bonded vicinal silanols (Scheme 2). Fumed silica, which is synthesized at ∼1300 °C in a high partial pressure of water,[3] has a lower total hydroxyl content (2.8 OH/nm^2 as also reported for laboratory-prepared fumed silica,[48]) but isolated silanols constitute about 10% of the surface. For both Stöber and fumed silica NPs, heat treatment causes a progressive dehydroxylation of the silica surface via condensation reactions of adjacent surface silanols (≡Si−OH + HO−Si≡ ⇔ ≡Si−O−Si≡), as is well documented for colloidal silica[5,49,50] and silica gels.[4] Because "as-received" fumed silica has a lower total hydroxyl content and a greater proportion of isolated hydroxyls than Stöber silica, it undergoes less thermally promoted dehydroxylation over the temperature range 200−800 °C.

In order to assess the potential of fumed silica or Stöber silica NPs to generate hydroxyl radicals, we performed electron paramagnetic resonance (EPR) studies after thermal annealing or rehydration. SI Figure S2 shows the surface area normalized EPR spectra, where we observe the 1:2:2:1 quartet characteristic of DMPO−$OH^{\bullet}$, whose intensities are indicative of the respective reactivities of surface defects with H_2O_2 or water to produce hydroxyl radicals ($OH^{\bullet}$) according to a *Fenton-like* reaction.[9,51] For all treatment conditions, we observe fumed silica to have a much greater ability to generate hydroxyl radicals, $OH^{\bullet}$, than Stöber silica NPs.

Analysis of the spectroscopic data along with the specific surface area allowed determination of the thermal and environmental treatment dependence of the key physicochemical properties of the fumed and Stöber silica samples. Figure 3 A-D reports the BET surface area and the surface area normalized concentrations of total, isolated and hydrogen bonded silanols and potential to generate hydroxyl radicals. Because three- and four-membered siloxane rings can form both within the bulk and on the surface, their relative proportions were determined by integration of the respective Raman bands and normalization by a band attributed to the total siloxane concentration. Upon thermal treatment to 600 °C, Stöber silica NPs experience a substantial loss of surface area (Figure 3A) and roughness (Figure 2A) attributed to continued condensation reactions of their silica cores consistent with reduced concentrations of total and hydrogen-bonded silanols (Figure 3B). Over the same temperature range fumed silica NPs exhibit approximately constant surface area (Figure 3A) and maintain smooth surfaces (Figure 2A) as expected based on their formation and quenching from high temperature. Additionally over the complete temperature range, both fumed and Stöber silica NPs undergo progressive surface dehydroxylation, contributing additionally to reductions of their respective total and hydrogen-bonded silanol concentrations (Figure 3B). Condensation of surface hydrogen-bonded silanols serves to increase the proportion of remaining isolated silanols, which for Stöber silica NPs first appear at 200 °C and increase progressively to 800 °C. In comparison, "as-received" fumed silica has an isolated silanol concentration of 0.3 OH/nm^2, which increases further to 400 °C and then remains nearly constant. For fumed silicas synthesized at high temperature and having a fully condensed silica core, dehydroxylation necessarily leads to the formation of mostly surface-associated siloxane rings, while, for Stöber silica, condensation occurs both within the bulk to form mainly unstrained 5-membered and larger rings (∼430 cm^{-1} Raman band) and on the surface to form 3MR (600 cm^{-1}, Scheme 4), which are absent below 200 °C. For both types of silica NPs, concentrations of strained three-member rings are maximized at intermediate temperatures (Figure 3C) due to their formation by thermally promoted condensation of isolated surface silanols (Scheme 4). Above 600 °C surface annealing occurs[52] in which surface-bound strained rings are removed through homolytic or heterolytic cleavage, with reformation of siloxane bonds. A major distinction is that fumed silica has both bulk (intrinsic) and surface associated 3MRs. Interestingly the thermal-dependence of the proportion of 3MRs appears to correlate with the potential to generate hydroxyl radicals (Figure 3D) increasing and then decreasing with heat treatment to 800 °C. Due to ring strain (as opposed to mechanical grinding), 3MRs could serve as precursors to oxyradicals (also known as nonbridging oxygen hole centers, Scheme 3) formed by homolytic cleavage of siloxane bonds.[53] Oxyradicals are reported to undergo further exothermic reactions with water to form hydroxyl radicals.[54,55]

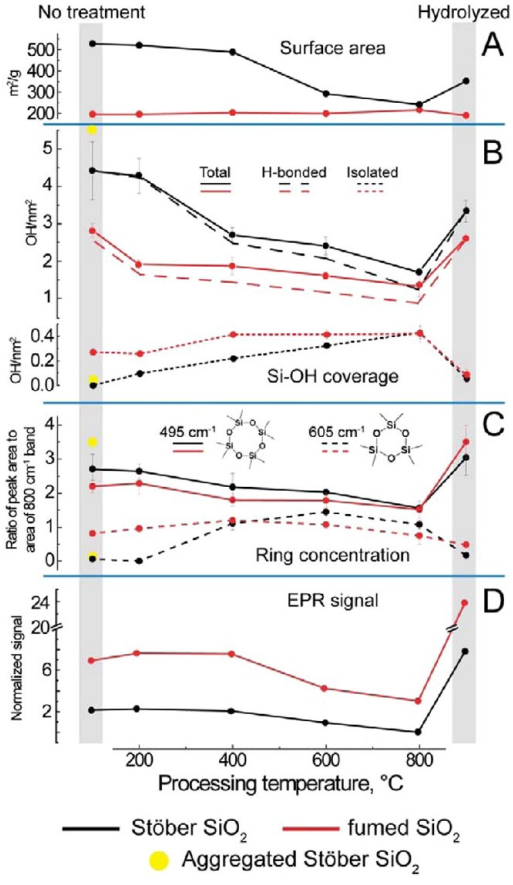

Figure 3. Comparison of physicochemical data for Stöber and fumed silica "as-received" or "as-prepared" (No treatment column) and after heat treatments up to 800 °C followed by rehydration (Hydrolyzed column). (A) Surface areas obtained using BET analysis of nitrogen adsorption data. (B) Silanol concentration calculated through the integration of the FTIR bands at ~3750 cm^{-1} (isolated) and 4500 cm^{-1} (total silanols). Hydrogen-bonded silanols are calculated by difference. (C) Relative four- and three-membered ring concentration in silica samples obtained from peak fitting of Raman data and normalization to the 800 cm^{-1} band attributable to the total siloxane content. (D) EPR data, normalized to sample surface area, of spin trap/silica solutions used to measure relative efficiency of hydroxyl radical generation. Yellow dots show hydroxyl concentrations and Raman data for colloidal silica aggregates.

Scheme 4. Formation of Strained Three-Membered Siloxane Rings on the Silica Surface via Thermally Promoted Dehydroxylation

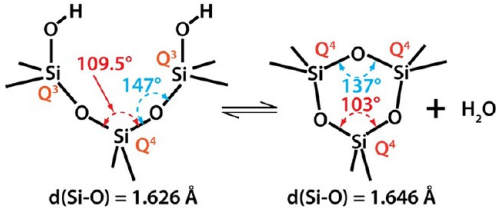

Upon rehydration silica nanoparticle surfaces undergo progressive stages of siloxane bond hydrolysis, increasing the total silanol concentration and decreasing the proportion of isolated silanols (Figure 3B, hydrolyzed). Surface-associated 3MRs are hydrolyzed (reverse of Scheme 4)[25] as evident in Figure 3C, while bulk, intrinsic 3MRs are preserved and could become exposed at the particle surface the finite population of 3MRs for rehydrated fumed silica (Figure 3C) is evidence of such an intrinsic population of 3MRs formed at very high temperature and 'frozen-in' by rapid thermal quenching. The potential to generate hydroxyl radicals is increased upon rehydration, particularly for fumed silica NPs.

3.2. Single and Multiparameter Cytotoxicity Assays and Red Blood Cell Lysis Demonstrate Differences in the Toxicity Potential of Different Types of Silica Nanoparticles. To benchmark the relative toxicities of the various silicas, the cellular viability of BEAS-2B or RAW 264.7 cells was assessed by LDH, MTS, and ATP assays upon exposure to a spectrum of amorphous (fumed, Stöber, and mesoporous) and crystalline (Min-U-Sil and silicalite) silica NPs. The cells were treated with silica nanoparticles for 24 h over a wide dose range (0.4–200 $\mu g \cdot mL^{-1}$). We observed that fumed silica and nanosized Min-U-Sil could induce a robust decline in cell viability and cellular ATP levels as well as the increased LDH release in BEAS-2B as well as RAW 264.7 cells, while Stöber silica, mesoporous silica, and silicalite had insignificant effects on these toxicological parameters (Figure 4A, SI Figure S3).

We also performed toxicological comparisons of the nanoparticles using our multiparametric HTS assay that assesses contemporaneously a number of oxidative stress parameters at multiple doses (0.4–200 $\mu g \cdot mL^{-1}$) and time points (1–6 and 24 h). Oxygen radical generation, cell membrane damage, intracellular calcium influx and dissipation of mitochondrial membrane potential are determined using the fluorescent dyes MitoSox Red, DCF, PI, Fluo-4, and JC-1, respectively. This assay is carried out by automated epifluorescence microscopy using threshold levels to score the % positive cells for each parameter as described in the Materials and Methods section. Statistical analysis of the rich data content by the strictly standard mean deviation (SSMD) method allowed us to generate heat maps, which provide hazard ranking of the different silica nanoparticles in relation to untreated (control) cells (Figure 4B, SI Figure S4). The red pixels in the heat map indicate significant toxicity, while blue pixels indicate no significant response generation. The heat maps presented in Figure 4B and Figure S4 for BEAS-2B and RAW 264.7 cells, respectively, show that fumed silica and nanosized Min-U-Sil induced robust increases in cell membrane permeability, intracellular calcium flux, and superoxide generation. Additionally, the heat map shows that fumed silica could induce mitochondrial depolarization.

In addition to cytotoxicity screening, we also performed a red blood cell (RBC) lysis assay. Mouse RBCs were exposed to 25, 50, and 100 $\mu g \cdot mL^{-1}$ of each of the particle types, and the hemoglobin release in the supernatant due to RBC lysis was evaluated by a colorimetric assay (Figure 4C) quantified spectroscopically by absorbance at 541 nm (Figure 4D). Panels C and D of Figure 4 show that fumed silica and nanosized Min-U-Sil result in extensive dose-dependent RBC lysis, whereas Stöber, mesoporous, and silicalite nanoparticles resulted in negligible membrane damage over the same NP concentration range.

3.3. Hydration-State Dependence of Silica Nanoparticle Toxicological Potential. Since microsized Min-U-Sil is known for its hazardous properties, including the ability to generate free radicals (Scheme 3),[9,15,56] the demonstrated toxicity of nanosized quartz was not unexpected. However, the significantly greater toxicity of fumed silica compared to that of

dx.doi.org/10.1021/ja304907c | J. Am. Chem. Soc. 2012, 134, 15790–15804

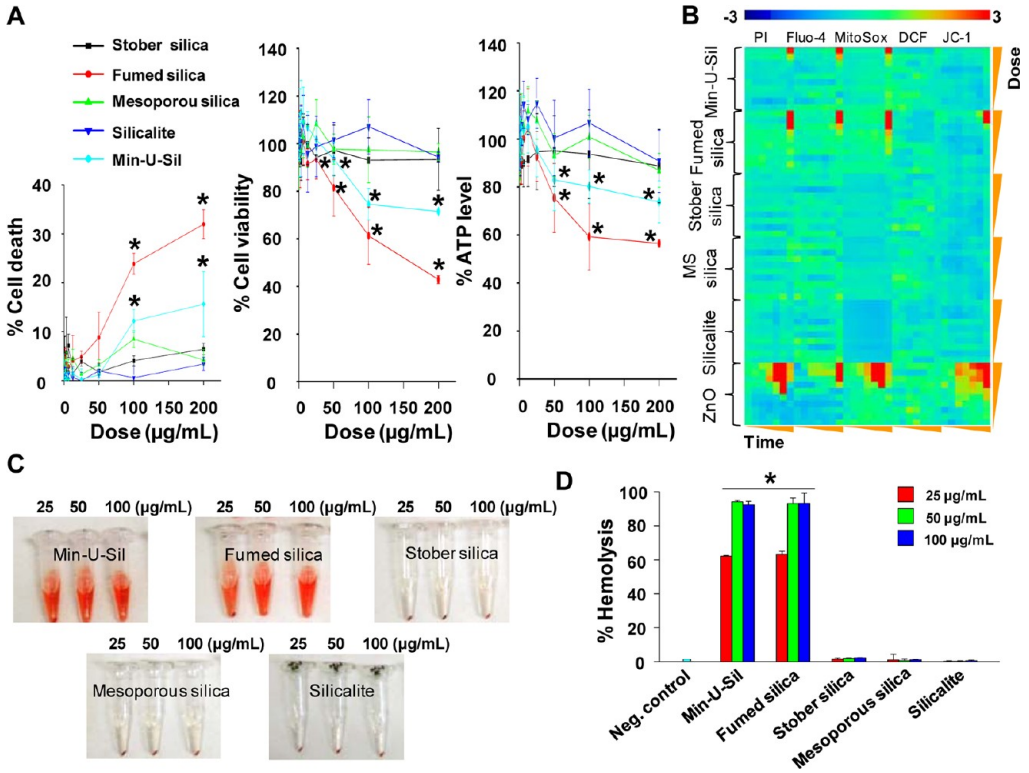

Figure 4. Toxicity profiles of different amorphous and crystalline silica nanoparticles. (A) Cytotoxicity of silica nanoparticles assessed in BEAS-2B cells. Cell death, cell viability, and ATP level were determined by LDH, MTS, and ATP single-parameter assays and shown in left, middle, and right-hand panels, respectively. This experiment was performed by introducing a wide dose range (400 ng/mL to 200 $\mu g \cdot mL^{-1}$) of each material to 10,000 cells grown in 96-well plates overnight and then performing the assays with commercial kits as described in Materials and Methods. (B) Heat maps to compare the toxic oxidative stress potential of silica nanoparticles in BEAS-2B cells using the multiparameter HTS assay. The heat maps were established using SSMD statistical analysis to evaluate the supra-threshold cellular responses by automated epifluorescence microscopy. The response parameters included measurement of intracellular calcium flux (Fluo-4), ROS generation (MitoSox Red and DCF), and mitochondrial membrane depolarization (JC-1). Cells were treated with a wide dose range of silica nanoparticles, beginning at 400 ng/mL and then doubling the dose up to 200 $\mu g \cdot mL^{-1}$. Epifluorescence images were collected hourly for the first 6 h and then again at 24 h. (C) Hemolysis activity of silica nanoparticles. Mouse RBCs were exposed to silica nanoparticles for 3 h, and the released hemoglobin from cells appears as red color in the supernatant. (D) Quantitative analysis of the percentage of released hemoglobin as shown in (C). The released hemoglobin was determined through measuring the absorbance of the supernatant at 541 nm, and the percentage of the released hemoglobin was calculated as described in Materials and Methods. *$p < 0.05$ compared with control.

Stöber silica (Figure 4) was unexpected, as both materials are amorphous and of comparable primary particle size. In order to further explore this difference, we hypothesized that the differences in silica ring distribution and surface silanol display (Figures 2 and 3) could underlie the toxicological differences in these amorphous materials. To test this hypothesis, both fumed and Stöber silica NPs were annealed at 600 or 800 °C to understand how progressive dehydroxylation and siloxane framework reconstruction (B and C of Figure 3) affect cell viability (Figure 5A) and RBC lysis potential (Figure 5B). Heating of fumed silica to 600 and 800 °C reduced the surface area normalized total hydroxyl content (Figure 3B), which was accompanied by decreased cytotoxicity in BEAS-2B (Figure 5A) and RAW cells (SI Figure S5). Heat treatment also reduced RBC hemolysis compared to the "as-received" fumed silica (Figure 5B and C [left panel]). We then asked whether rehydration of the fumed silica sample would cause recovery of the nanoparticle hazard potential. Indeed, rehydration of the 800 °C sample, which increased the total and hydrogen-bonded silanol concentrations to approximately those of the "as-received" fumed silica sample was accompanied by an increase in cytotoxicity and hemolytic activity to levels comparable to or exceeding those of the parent "as-received" sample (Figure 3B). In contrast to fumed silica, heating and rehydration of Stöber silica, which significantly reduced and then increased the surface area normalized hydroxyl content (Figure 3B), had no significant impact on cell viability (Figure 5A). Figure 5C shows that these treatments resulted in a dose-dependent decrease and an increase in RBC lysis (B and C [right panel] of Figure 5), but these effects were minimal (<2%) compared to those of fumed silica (Figure 5C [left panel]).

3.4. Fumed and Stöber Silica Differ with Respect to Activation of the Nalp3 Inflammasome and IL-1β Production in THP-1 Cells. Previous studies looking at the pulmonary toxicity of alpha-quartz, have demonstrated the involvement of IL-1β production in the pathogenesis of pulmonary fibrosis.[30,57,58] Moreover, there is increasing evidence that IL-1β release in phagocytic cells by substances such as quartz and asbestos involves activation of the Nalp3 inflammasome.[58,59] In order to understand whether fumed silica was capable of activating the same pathway, THP-1 cells, which is a macrophage-like cell line commonly used to assess inflammasome activation,[24] were exposed to fumed and Stöber silica for 24 h, using a range of doses (0.4–200 $\mu g \cdot mL^{-1}$). Cellular supernatants were collected for measurement of IL-1β levels by ELISA. Figure 6A shows "as-received" fumed silica

dx.doi.org/10.1021/ja304907c | J. Am. Chem. Soc. 2012, 134, 15790–15804

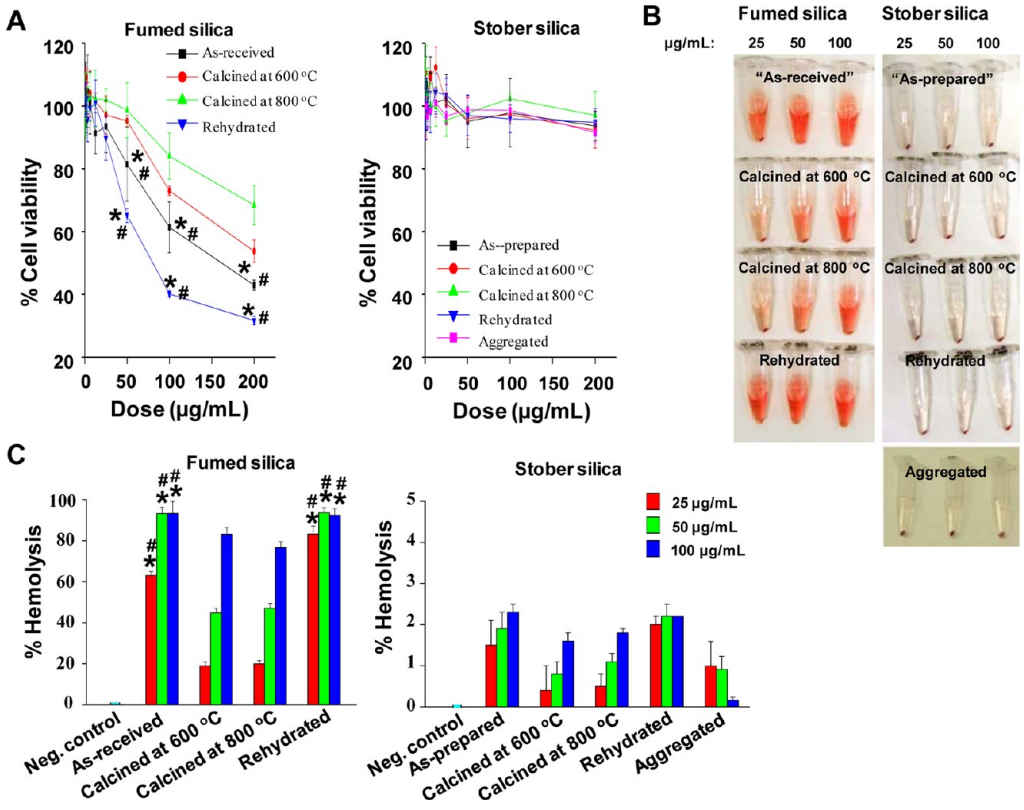

Figure 5. Toxicity profiles of fumed and Stöber silica nanoparticles processed under different conditions. (A) Cytotoxicity assessment of a series of fumed silica (left-hand panel) and Stöber silica (right-hand panel) nanoparticles in BEAS-2B cells. Cells were treated with a wide dose range (400 ng/mL to 200 $\mu g \cdot mL^{-1}$) of nanoparticles for 24 h, and cell viability was assessed by the MTS assay. Nanoparticles calcined at 600 or 800 °C were synthesized by heat treatment at the respective temperatures for 6 h followed by redispersion. Rehydrated nanoparticles were synthesized by refluxing 800 °C treated nanoparticles in water for 24 h. Aggregated samples (Figure 1C) were prepared by electrostatic destabilization of the parent Stöber silica NPs. (B) Hemolysis activity of a series of fumed and Stöber silica NPs. Mouse RBCs were exposed to "as-received" or "as-prepared" calcined and rehydrated fumed silica or Stöber silica for 3 h. Released hemoglobin appears as red color in the supernatant. (C) Quantitative analysis of the percentage of released hemoglobin as shown in B). The released hemoglobin was determined through measuring the absorbance of the supernatant at 541 nm, and the percentage of the released hemoglobin was calculated as described in Materials and Methods. * and # are defined as $p < 0.05$ compared with data of samples calcined at 600 or 800 °C, respectively, at the same doses.

induced a dose-dependent increase in IL-1β production in THP-1 cells, while "as-prepared" Stöber silica showed a minimal effect on IL-1β and no significant dose dependence. In order to demonstrate the involvement of the Nalp3 inflammasome, we used THP-1 cells with knock-down of the Nalp 3 and ASC genes and found IL-1β production to be nearly completely abolished (Figure 6B). Moreover, heat treatment decreased the ability of fumed silica to induce IL-1β release, while rehydration had the reverse effect (Figure 6A). In contrast, heat treatment and rehydration of Stöber silica nanoparticles had no significant effect on IL-1β cytokine production.

3.5. Fumed and Stöber Silica Differ in Their Ability to Induce Cathepsin B Release. Because activation of the Nalp 3 inflammasome by asbestos fibers and other long aspect ratio materials (e.g., carbon nanotubes and metal oxide nanowires) is attributed to lysosomal damage and cathepsin B release,[39,40,59,60] we asked whether fumed silica similarly induces lysosomal damage. This was assessed using confocal microscopy to determine intracellular localization of Magic Red, a cathepsin B substrate. As shown in Figure 6C, untreated THP-1 cells showed a punctate Magic Red fluorescence indicative of its containment in intact lysosomes, while three different long aspect ratio control materials (carbon nanotubes, TiO_2 nanobelts or CeO_2 nanowires) could be seen to disrupt the lysosomes, allowing Magic Red to be released to the cytosol. In contrast, neither "as-received" fumed nor "as-prepared" Stöber silica nanoparticles were capable of inducing cathepsin B release. This demonstrates that activation of the Nalp3 inflammasome by fumed silica proceeds via a nonlysosomal mechanism. This prompted us to study the cellular route of silica nanoparticle processing.

3.6. Differential Cellular Uptake and Distribution of Fumed and Stöber silica nanoparticles in BEAS-2B and THP-1 cells. In order to address the cellular uptake and fate of fumed silica and Stöber silica nanoparticles, confocal microscopy and TEM were performed in BEAS-2B and THP-1 cells, following exposure to 25 $\mu g \cdot mL^{-1}$ FITC-labeled or unlabeled nanoparticles, respectively. Confocal microscopy demonstrated that, while chainlike fumed silica aggregates tended to collect on the outer cell membrane of both cell types (Figure 7A and SI Figure S6A), Stöber silica nanoparticles were taken up in these cells (Figure 7B and SI Figure S6B). This difference in cellular processing was confirmed by TEM, which demonstrated that fumed silica NPs were mostly associated with the external cell surface membrane, where the particles stimulated filapodia formation and membrane ruffling (Figure 7C). Relatively few fumed silica nanparticles were taken up in the cell. In contrast, TEM imaging shows that most Stöber silica NPs are internalized and do not collect on the surface

dx.doi.org/10.1021/ja304907c | J. Am. Chem. Soc. 2012, 134, 15790−15804

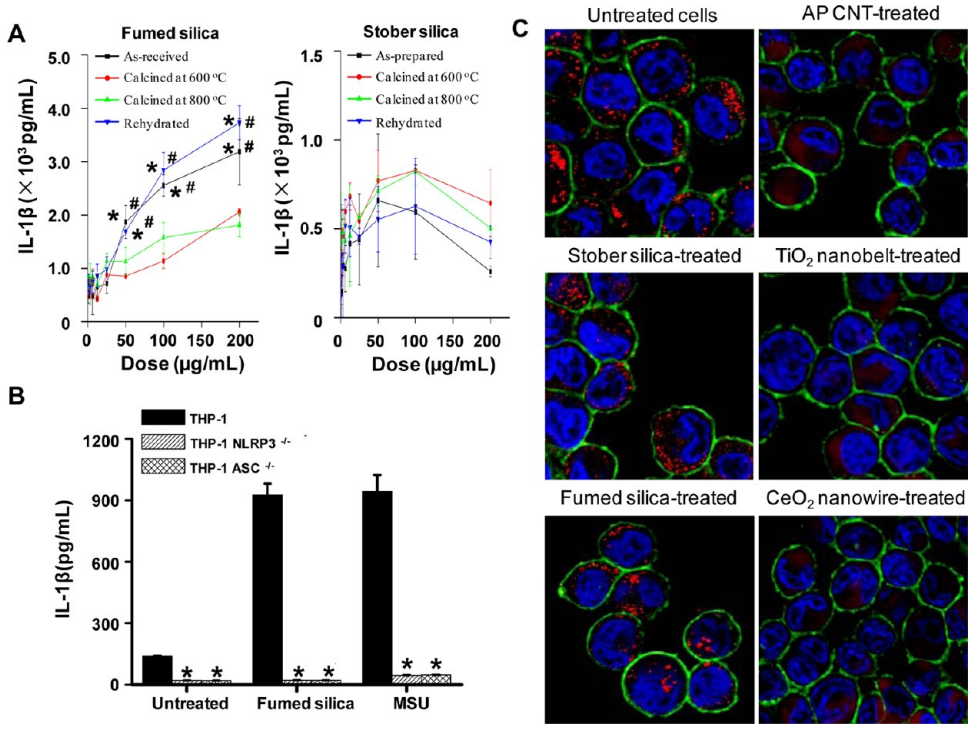

Figure 6. Potential toxicity mechanism of fumed silica. (A) Different IL-1β induction by fumed and Stöber silica processed under different conditions in THP-1 cells. The PMA-differentiated THP-1 cells were treated with a wide dose range (400 ng/mL to 200 $\mu g \cdot mL^{-1}$) of nanoparticles for 24 h, and the generated IL-1β was determined through an ELISA assay. * and # are defined as $p < 0.05$ compared with data of samples calcined at 600 or 800 °C, respectively, at the same doses. (B) Low IL-1β induction by fumed silica in Nalp 3- and ASC-knock down THP-1 cells. The PMA-differentiated THP-1, Nalp-3-knock down THP-1 and ASC-knock down THP-1 cells were treated with 25 $\mu g \cdot mL^{-1}$ of fumed silica for 24 h, and the generated IL-1β was determined through an ELISA assay. Monosodium urate crystals (MSU) were used as a positive control. *$p < 0.01$ compared with the values in THP-1. (C) Confocal microscopy images showing cathepsin B lysosomal release in THP-1 cells. The PMA-differentiated THP-1 cells were treated with 25 $\mu g \cdot mL^{-1}$ of nanomaterials for 5 h, and cathepsin B, cell membrane, and nuclei were stained with Magic Red, Alexa 488-conjugated wheat germ agglutinin (WGA), and Hoechst 33342, respectively. Cathepsin B in intact lysosomes exhibits punctate red fluorescence as shown in untreated, Stöber silica-treated and fumed silica-treated cells, whereas damaged lysosomes led to cathepsin B release into the cytosol, evident as diffuse red fluorescence, in carbon nanotube (AP CNT)-treated, TiO_2 nanobelt-treated, and CeO_2 nanowire-treated positive control cells.

membrane and that the membrane is comparatively devoid of membrane ruffles (Figure 7D).

4. DISCUSSION

As reviewed by Nel et al.,[27] nanoparticle interactions at the nano/bio interface are governed by a spectrum of biophysicochemical properties that include the material's chemical composition, surface functionalization, shape, angle of curvature, porosity, crystallinity, heterogeneity, roughness, and hydrophobicity or hydrophilicity. It is not a surprise therefore that materials, with nominally the same chemical composition, can interact differently with biomolecules and cellular components and show different toxicity behaviors. These differences are often diminished or vanish when NP toxicity behaviors are normalized on the basis of particle size or total accessible surface area. However, for amorphous silica the low free energy landscape of siloxane configurations results in a continuum of framework and surface structures that are highly dependent on the processing pathway. As we show, amorphous silica nanoparticles with nearly identical primary particle sizes can have significantly different surface areas, states of aggregation, framework structures, degree and patterns of hydroxylation, as well as hydrogen bonding. Even when normalized to accessible surface area, these differences persist and influence toxicological behavior.

Fumed silica and colloidal silica nanoparticles, although amorphous, are distinguished by their completely different synthesis mechanisms. Fumed silica is produced by the vapor phase hydrolysis of silicon tetrachloride vapor in a hydrogen–oxygen flame at high temperature (~1400–1800 °C)[3] and generally attributed to the reactions:

$$2H_2 + O_2 \rightarrow 2H_2O \quad (1)$$

$$SiCl_4 + 2H_2O \rightarrow SiO_2 + 4HCl \quad (2)$$

$$SiCl_4 + 2H_2O \rightarrow SiO_2 + 4HCl \quad (\text{Net})$$

It results in highly coalesced, chainlike aggregates of small silica nanoparticles (Figure 1B), whose primary particle sizes range from about 10–20 nm, depending on $SiCl_4$ concentration and flame conditions.[3,42] The commonly written net reaction is misleading in that the reaction is conducted within a synthesis environment containing up to 30 mol % H_2O, causing the 'SiO_2' to be hydrated (and therefore hydrophilic) with hydroxyl contents[48] equivalent to 2–3 OH/nm^2 as shown in Figure 3B ('No treatment'). Additionally, the silica nanoparticles are rapidly solidified at room temperature, freezing in a structure representative of that existing at a much higher fictitious or so-called *fictive* temperature. Raman spectroscopy can distinguish between two-, three-, four-, and five or more-membered siloxane rings on the basis of their symmetric oxygen ring breathing modes.[25] As shown in Figures 2C and 3C, "as-

dx.doi.org/10.1021/ja304907c | J. Am. Chem. Soc. 2012, 134, 15790–15804

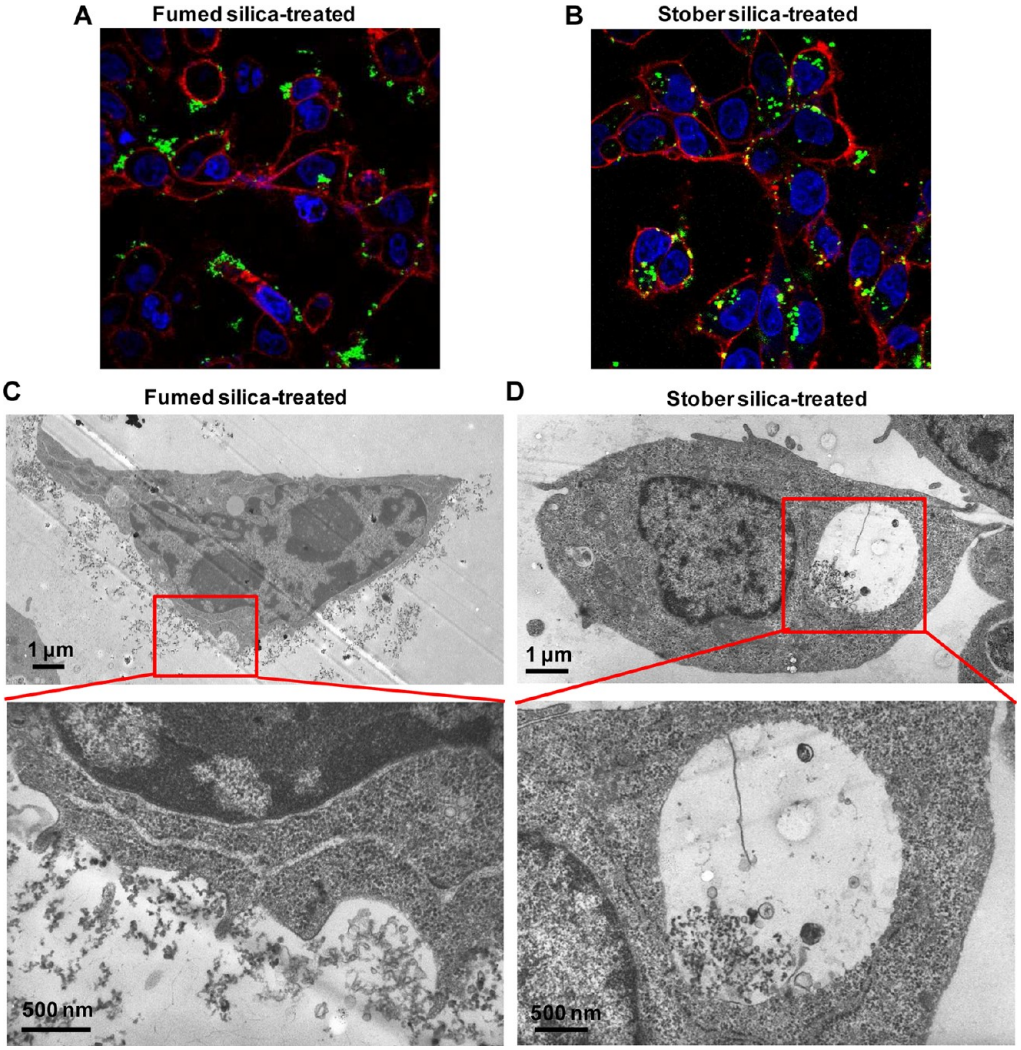

Figure 7. Differential cellular distribution of fumed and Stöber silica NPs in BEAS-2B cells. (A) Confocal microscope image of fumed silica-treated cells. (B) Confocal microscope image of Stöber silica-treated cells. (C) TEM image of fumed silica-treated cells. (D) TEM image of Stöber silica-treated cells. For confocal microscope images, BEAS-2B cells were treated with 25 $\mu g \cdot mL^{-1}$ FITC-labeled fumed or Stöber silica for 5 h. After fixation, cell membrane was stained by Alexa Fluor 594-conjugated WGA to show red fluorescence, while nuclei were stained with Hoechst 33342 to show blue fluorescence. Most green fluorescent FITC-labeled fumed silica NPs appear adherent to the cell membrane, while most FITC-labeled Stöber silica NPs appear internalized. For TEM images, BEAS-2B cells were treated with 25 $\mu g \cdot mL^{-1}$ fumed or Stöber silica for 5 h. Representative TEM images showed that most fumed silica NPs were found adherent to the cell membrane, while most Stöber silica NPs were found to be internalized into cells.

received" fumed silica has an intrinsic population of energetic, small strained 3MRs established at high temperature and 'frozen-in' by rapid quenching that greatly exceeds that of "as-prepared" colloidal silicas, bulk amorphous silica glass,[45] and all crystalline forms of silica (SI Figure S1). EPR studies of γ-irradiated silica gels further associate strained 3MRs with paramagnetic E' and nonbridging oxygen hole centers (oxy-radicals)[53,61] that form via homolytic cleavage of siloxane bonds (Scheme 3) and can react with water to produce hydroxyl radicals.[54,55] Additionally the high fictive temperature creates a population of isolated silanol groups whose temperature dependence differs from that of colloidal silicas (Figure 3B).

Colloidal silica NPs, including Stöber silica, LUDOX, and mesoporous silica, are produced by successive molecular condensation reactions of soluble silanol species conducted in water or alcohol/water media under basic conditions at temperatures generally below 150 °C:

$$\equiv Si{-}OH + HO{-}Si\equiv \Leftrightarrow \equiv Si{-}O{-}Si\equiv + H_2O \quad (4)$$

In this case, the developing framework topology remains in reversible equilibrium with water and is therefore essentially devoid of hydrolytically unstable, small strained 2 and 3MRs[4] and isolated silanols as shown for Stöber silica NPs (Figures 2C and 3C, 'No treatment' and SI Figure S1). Reaction-limited nucleation and growth results in discrete nanoparticles whose interiors range from substantially anhydrous SiO_2 (high $pH/T/[H_2O]$) to somewhat hydrated (lower $pH/T/[H_2O]$).[5]

For both fumed silica and colloidal silica nanoparticles, annealing at temperatures up to 800 °C decreases the surface hydroxyl coverage due to condensation reactions of neighboring silanol groups to form siloxane bonds (eq 4)—the same reaction that forms siloxane bonds in solution. Physically bound water and hydrogen-bonded silanols are removed first (Figure 3B), creating closed siloxane rings and progressively increasing surface hydrophobicity. Distinct from aqueous solution conditions, thermally promoted condensation reactions can

dx.doi.org/10.1021/ja304907c | J. Am. Chem. Soc. 2012, 134, 15790−15804

result in the formation of strained surface-associated 3MRs (Scheme 4) as evident in Figure 3C for Stöber and fumed silica NPs annealed at intermediate temperatures (400 and 600 °C). As previously shown for high surface area silica gels, upon re-exposure to water, these surface-associated strained rings are rapidly hydrolyzed (Figure 3C (Hydrolyzed)) via dissociative chemisorption of water (see Scheme 5).[25,62] For Stöber silica NPs, this practically eliminates 3MRs, but for fumed silica there remains an intrinsic population of 3MRs (Figure 3C "as received").

Scheme 5. Siloxane Bond Hydrolysis via Dissociative Chemisorption of Water

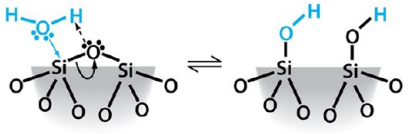

The physicochemical differences in fumed silica and Stöber silica nanoparticles are manifested in distinctly different patterns of inflammation, toxicity, and hemolysis. As shown clearly by the dose-dependence of cell viability, red cell membrane lysis (Figure 5) and secretion of the pro-inflammatory cytokine IL-1β (Figure 6), along with the multiparameter oxidative stress (Figure 4B and SI Figure S4) assays, the "as-received" fumed silica and "as-prepared" Stöber silica nanoparticles have considerably different toxicity potentials. While Stöber silica has minimal overall toxicity and hemolytic activity for doses up to 200 $\mu g \cdot mL^{-1}$, fumed silica showed robust, dose-dependent toxicity and hemolytic activity, even exceeding that of the positive control Min-U-Sil (Figures 4, SI Figures S3 and S4) in epithelial cells and macrophages. By way of comparison, dose dependent toxicity and hemolytic activity of amorphous silica NPs have been reported at concentrations up to 2500 $\mu g \cdot mL^{-1}$, covering the range studied here.[18−21,23,63] Although results are variable (because of differing physicochemical properties), it is noteworthy that Napierska et al studied Stöber silica nanoparticles processed under dilute conditions using dialysis, allowing assessment of the toxicity of individual well-dispersed nanoparticles. Over the concentration range 0−200 $\mu g \cdot mL^{-1}$ studied by us, they observed less than 10% cytoxicity for particles >60-nm in diameter, while for 16-nm NPs they observed an increase in toxicity from 10 to 80% over the concentration range 50−200 $\mu g \cdot mL^{-1}$. As the Stöber silica NPs in our study are prepared by drying, heating, and redispersion, they are compact aggregates with hydrodynamic diameters exceeding 60-nm (as shown in Figure 2 and SI Table S1). Their very low toxicities are thus consistent with literature results. In contrast, we find fumed silica, thermally treated and dispersed under identical conditions to Stöber silica, to be very highly cytotoxic and hemolytically active. Although described as amorphous silica,[22] Slowing et al. report hemolytic activity of what appear to be large fumed silica aggregates and find nearly 50% hemolysis for particle concentrations of 100 $\mu g \cdot mL^{-1}$. This is suggestive that, despite its large aggregate size, fumed silica can have a high toxicity potential consistent with our results.

In order to further understand the striking differences in toxicity between fumed and Stöber nanoparticles and establish needed SARs for amorphous silicas, we characterized the biological behaviors of Stöber and fumed silica following thermal annealing and rehydration. As shown in Figure 5A and B, progressive dehydroxylation (Figure 3B) of fumed silica during heating resulted in a statistically significant increase in viability and reduction in hemolysis. Figure 6A shows that the increase in viability is accompanied by a decrease in the secretion of IL-1β. In contrast, for Stöber silica NPs, which showed minimal toxicity under all treatment conditions, thermal annealing had a statistically negligible effect on viability and IL-1β generation and resulted in only a modest reduction in % hemolysis.

It is now generally accepted that NP toxicity depends on three interrelated factors: the intrinsic toxicity and reactivity of the material, its surface area and surface chemistry in contact with the cell, and its morphology (size, shape, state of aggregation). Here we compare pure amorphous silca nanoparticles with nominally the same composition and primary particle size. Both Stöber and fumed silica dissolve to form monosilicic acid or oligosilicic acid, which has been shown to have no intrinsic toxicity.[20] Both materials have similar settling velocities (SI Figure S7A and B), so the cellular assays are based on comparable contact with the particles. Thus, the differences in toxicity behaviors we observed should be attributable to differences in surface chemistry, reactivity, and/or NP morphology. Silica surface chemistry is governed by the concentration of hydroxyl groups (Scheme 2) and surface defects (Scheme 3). As discussed extensively in the literature, surface silanol groups ($\equiv$Si−OH) selectively promote interactions with cell membranes and have been implicated in the hemolytic activity and cytotoxicity of silica.[18,22,64−67] Silanols serve as hydrogen donors with quaternary and phosphate ester groups of phospholipid membrane components or to lesser extent secondary amide groups of proteins.[22,28] Moreover, anionic deprotonated silanols interact electrostatically with positively charged tetraalkylammonium-containing phospholipids.[68] The trend of decreased lysis of RBCs with increasing treatment temperature and extent of dehydroxylation observed for fumed silica, and to a much lesser extent Stöber silica NPs (Figure 5B and C), is therefore consistent with the generally held view that hemolytic activity of silica is related to specific interactions with surface silanol groups.[18,22,64−67] Comparing Figures 5A and C we find that RBC hemolytic activity is reasonably predictive of cytotoxicity (compare A and C of Figure 5). What is not evident is why the fumed silica NPs, whose total silanol concentration is less than or equal to that of Stöber silica for all treatment temperatures and conditions, has a dramatically higher cytotoxicity. Comparison of the fumed and Stöber silica NP data in Figure 5C shows that the temperature and dose dependence of red cell lysis is greatly amplified by the fumed silica samples relative to Stöber silica NPs. The 800 °C-treated fumed silica and Stöber silica samples in particular, whose total, isolated and hydrogen-bonded silanol concentrations, primary particle size, and specific surface areas are nearly identical, emphasize that surface silanol concentration alone is not predictive of lysis and viability.

A second determinant of surface reactivity and a potential contributory factor to silica toxicity is ROS production.[10,54] Plasma membranes and RBCs are susceptible to oxidative damage, which leads to peroxidation of the membrane lipids, hemolysis, and alteration in activity of antioxidant enzymes catalase and superoxide dismutase.[69,70] Our EPR results show fumed silica to be a potent generator of hydroxyl radicals compared to colloidal silica (SI Figure S2). While the ability of

surface defects or iron impurities to produce ROS in natural crystalline quartz[9,10,5159] is well established and has been implicated in silicosis,[59] the ability of ultrapure amorphous silica to produce ROS has only recently been recognized. Ghiazza et al.[6] reported hydroxyl radical formation for submicrometer powders prepared by grinding high purity silica glass made by conventional high-temperature synthesis but not for commercial amorphous silica of comparable particle size. Morishige et al.[24] reported ROS production for commercial 1-μm diameter spherical amorphous silica (no physicochemical properties reported). Most relevantly Thomassen et al. (2009)[21] compared colloidal Stöber and LUDOX nanoparticles with different diameters using the spin-trap method. They observed modest levels of hydroxyl radical generation and determined the activity per square meter of exposed silica surface area to be independent of particle size and preparation method, suggestive of surface-associated defects. Our results represent the first systematic study of the synthesis, thermal treatment and hydration dependence of ROS generation for amorphous silica nanoparticles and emphasize the unusual ability of fumed (compared to colloidal) silica to generate hydroxyl radicals. For fumed silica, the thermally induced changes in hydroxyl radical generation (untreated −800 °C) mirror the relative concentrations of strained 3MRs (Figure 3C and D). 3MRs have been established as precursors of oxyradicals (Scheme 3)[53,61] which in turn are predicted and observed to react with water exothermically to form hydroxyl radicals.[54,55] We suggest that ring strain (as opposed to or in addition to mechanical grinding) results in preferential hemolytic cleavage of 3MRs to form surface radicals that can further react with water, oxygen, or hydrogen peroxide to generate hydroxyl radicals. A plausible reaction pathway is proposed in Scheme 6.

Scheme 6. Proposed Reaction Pathway for the Generation of ROS from 3MRs

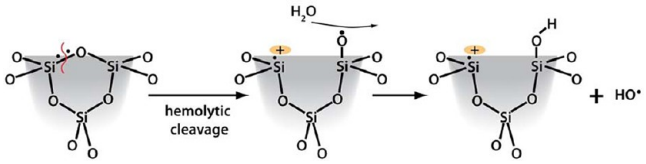

As surface 3MRs (Scheme 4) rapidly hydrolyze and can be thermally annealed at high temperature, their contribution to ROS generation is at present uncertain. However, it is important to note that fumed silica, in contrast to colloidal Stöber silica, has both surface and intrinsic (bulk) 3MRs (Figure 3C). Whereas surface 3MRs are rapidly hydrolyzed, intrinsic 3MRs can serve as a reservoir for ROS that can be continually exposed during prolonged hydration (rehydrated sample Figure 3D).

A third determinant of surface reactivity and potential toxicity is NP morphology. Fumed silica is composed of ramified and highly fused chainlike aggregates (Figure 1) characterized by a fractal dimension d_f = 2.1 (Figure 2), whereas Stöber silica NPs are discrete spherical particles (Figure 1) weakly aggregated into compact aggregates (Figure 2). Here it might be anticipated that the chainlike morphology of the fumed silica aggregates would be interpreted by the cells as a material with increased aspect ratio, stimulating filapodia formation on the membrane and internalization by macropinocytosis, as observed for mesoporous silica rods.[71] However as evident in the TEM images presented in Figure 7C for BEAS-2B cells, the highly ramified chainlike aggregates interfered in fumed silica nanoparticle uptake, causing trapping at the cell surface membrane.[59] In contrast as shown in Figure 7D Stöber silica NPs are internalized, presumably by an endocytotic or pinocytotic pathway, and processed into large vacuoles. Both filopodia formation and endocytosis depend on noncovalent interactions between surface silanols and the cell membrane.[22] In RBCs these noncovalent membrane interactions presumably result in membrane lysis,[22,72] helping to explain the hydroxyl concentration dependence of toxicity and hemolysis.

In an effort to assess whether aggregation alone could induce toxicity or hemolysis, Stöber silica NPs were aggregated by electrostatic destabilization forming chainlike morphologies similar to fumed silica (Figure 1C). As shown in Figure 5A−C, the Stöber silica aggregates had no significant toxicity or hemolytic activity. Confocal imaging (SI Figure S8), however, showed that, unlike fumed silica aggregates, colloidal aggregates were internalized much like the parent Stöber particles. Because the interparticle necks formed by fusion at >1300 °C for fumed silica are expected to be much stiffer than the necks formed by electrostatic destabilization and room temperature aging for the colloidal aggregates, this suggests that beyond morphology, the mechanical stiffness of a nanoparticle or aggregate is influential in dictating cellular interactions and toxicity potential.

On the basis of our results, we conclude that the aggregated nature of fumed silica combined with its hydroxylated surface chemistry and ability to generate ROS confer to fumed silica a toxicological behavior with similarities and differences compared to asbestos and other long aspect ratio materials known to result in chronic lung damage.[59] As for asbestos, fumed silica is sensed as a danger signal by the Nalp3 infammosome, whose subsequent activation leads to IL-1β secretion (Figure 6). However unlike the generally accepted Nalp3 inflammasome activation pathway for crystalline silica, where particles are phagocytosed leading to lysosomal rupture and cathepsin B release,[73] we show Nalp3 inflammasome activation can occur without lysosomal damage. Our results support an alternative reactive oxygen species (ROS) model of inflammasome activation. We propose that, via principally hydrogen-bonding interactions, fumed silica aggregates damage cell membranes and stimulate ROS production, both of which would act as signals for inflammasome activation. Unlike asbestos where infammasome-activating ROS have been attributed to iron impurities and their ability to catalyze radical formation, fumed silica is essentially devoid of iron. NADPH oxidases, are a potential source of ROS in professional phagocytes and have been suggested to function in ROS-dependent activation by particulates.[73] Here we suggest strained siloxane rings as alternative source of ROS that could act alone or in combination with NADPH oxidases or other sources. Fumed silica possesses an intrinsic population of 3MRs that are largely absent in colloidal silicas, and serve as a reservoir for surface radicals formed by homolytic siloxane bond cleavage.

Implications/Future Directions. On the basis of results for Stöber and fumed silica NP toxicity, we can make several general comments about amorphous silica nanoparticle toxicity. First, this work supports the notion that crystallinity is not a prerequisite for robust silica toxicity.[7] We show that amorphous fumed silica nanoparticle aggregates can have toxicity levels comparable to or exceeding those of crystalline silica NPs.

Second, our study corroborates the strong interaction of surface silanols with the cell membrane – resulting in modest to robust hemolysis of RBCs, macropinocytosis of compact silica NP aggregates, and cell surface ruffling for chainlike aggregates. Heat treatments (or surface porosity in the case of mesoporous silica particles) that reduce the surface area normalized hydroxyl concentration reduce these interactions and correspondingly any associated toxicity. Similarly, coating with polymers[18] or lipid bilayers[74] shield hydroxyl/cellular interactions and accordingly suppress toxicity. Third, activation of the Nalp3 inflammasome and ensuing IL-1β secretion requires ROS production. Rather than damage to the lysosome as for long aspect ratio materials, strained three-membered siloxane rings formed at high temperature are a potential source of ROS—due to their hydrolytic instability, these strained rings are absent in all colloidal silicas (Stöber silica, mesoporous silica, LUDOX, silicalite, and silica gels) as evidenced by Raman spectroscopy (see SI Figure S1). Heat treatments create surface-associated 3MRs by condensation of silanol groups (Scheme 4) or during the high-temperature formation of fumed silica or vitreous silica by thermodynamic equilibration. Surface associated 3MRs are rapidly hydrolyzed upon re-exposure to water and pose little toxicological potential. However, bulk 3MRs found in high-temperature fumed silica and vitreous silica (SI Figure S1) can serve as a ROS reservoir during silica nanoparticle hydrolysis or dissolution, explaining the reported toxicity of vitreous silica.[6] Crystalline quartz and cristobalite do not have strained rings, however iron impurities in natural minerals can generate ROS via the Fenton reaction, and grinding of crystalline surfaces may create higher or longer lasting concentrations of surface radicals than achievable in amorphous silica NPs.[6]

■ ASSOCIATED CONTENT

Ⓢ Supporting Information

Detailed information regarding synthesis and characterization of the nanoparticle samples. Characterization data include: hydrodynamic diameter, ζ potential, Raman spectra, derivative EPR spectra, sedimentation velocity, toxicity assessment in RAW cells, differential cellular distribution in THP-1 cells, BEAS-2B cells, and THP-1 cells assessed by confocal microscopy. This material is available free of charge via the Internet at http://pubs.acs.org.

■ AUTHOR INFORMATION

Corresponding Author

cjbrink@sandia.gov

Notes

The authors declare no competing financial interest.

■ ACKNOWLEDGMENTS

Primary support was provided by the U.S. Public Health Service Grants, U19 ES019528 (UCLA Center for Nanobiology and Predictive Toxicology) and RO1 ES016746. This work was also supported by the National Science Foundation and the Environmental Protection Agency under Cooperative Agreement Number DBI-0830117. C.J.B. and D.D. acknowledge additional support from the U.S. DOE Basic Energy Sciences Materials Science and Engineering program, the Sandia National Laboratories LDRD program, and the NCI Cancer Nanotechnology Platform Partnership 109 Grant 1U01CA151792-01. M.L.K. acknowledges the National Institutes of Health (grant GM 057378) for financial assistance. This work benefited from the use of the Low-Q Diffractometer, LQD, at the Manuel Lujan, Jr. Neutron Scattering Center of the Los Alamos National Laboratory supported by the US. Department of Energy at Los Alamos National Laboratory operated by Los Alamos National Security LLC under contract number DE-AC52- 6NA25396. Fluorescent microscopy was performed at the CNSI Advanced Light Microscopy/Spectroscopy Shared Facility at UCLA.

■ REFERENCES

(1) Lutgens, F. K.; Tarbuck, E. J. *Essentials of Geology*; 7th ed.; Prentice Hall, 2000.
(2) Brinkmann, U.; Ettlinger, M.; Kerner, D.; Schmoll, R. In *Colloidal Silica: Fundamentals and Applications*; Bergna, H. E., Roberts, W. O., Eds.; CRC Press: Hoboken, NJ, 2005, p 575–588.
(3) Pratsinis, S. *Prog. Energy Combust. Sci.* **1998**, *24*, 197–219.
(4) Brinker, C. J.; Scherer, G. W. In *Sol-Gel Science: The Physics and Chemistry of Sol-Gel Processing*; Academic Press: San Diego, CA, 1990.
(5) Iler, R. K. *The Chemistry of Silica*; John Wiley and Sons: New York, 1979.
(6) Ghiazza, M.; Polimeni, M.; Fenoglio, I.; Gazzano, E.; Ghigo, D.; Fubini, B. *Chem. Res. Toxicol.* **2010**, *23*, 620–629.
(7) Trofymluk, O.; Levchenko, A. A.; Tolbert, S. H.; Navrotsky, A. *Chem. Mater.* **2005**, *17*, 3772–3783.
(8) Hobbs, L.; Yuan, X.; Qin, L.; Pulin, V.; Coventry, A. *Microsc Microanal* **2002**, *8*, 29–34.
(9) Fubini, B.; Hubbard, A. *Free Radical Biol. Med.* **2003**, *34*, 1507–1516.
(10) Schoonen, M. A. A.; Cohn, C. A.; Roemer, E.; Laffers, R.; Simon, S. R.; O'Riordan, T. *Reviews in Mineralogy and Geochemistry* **2006**, *64*, 179–221.
(11) Castranova, V.; Vallyathan, V. *Environ Health Perspect* **2000**, *108*, 675–684.
(12) Elias, Z.; Poirot, O.; DaniÄre, M. C.; Terzetti, F.; Marande, A. M.; Dzwigaj, S.; Pezerat, H.; Fenoglio, I.; Fubini, B. *Toxicol In Vitro* **2000**, *14*, 409–422.
(13) Donaldson, K.; Tran, C. L. *Inhalation Toxicology* **2002**, *14*, 5–27.
(14) Rimal, B.; Greenberg, A. K.; Rom, W. N. *Current Opinion in Pulmonary Medicine* **2005**, *11*, 169–173.
(15) Fubini, B. *The Annals of Occupational Hygiene* **1998**, *42*, 521–530.
(16) Fubini, B. In *The Surface Properties of Silica*; Legrand, A. P., Ed.; J. Wiley and Sons: Chichester, United Kingdom, 1998, p 415–464.
(17) Brunner, T. J.; Wick, P.; Manser, P.; Spohn, P.; Grass, R. N.; Limbach, L. K.; Bruinink, A.; Stark, W. J. *Environ. Sci. Technol.* **2006**, *40*, 4374–4381.
(18) Lin, Y.-S.; Haynes, C. L. *J. Am. Chem. Soc.* **2010**, *132*, 4834–4842.
(19) Maurer-Jones, M. A.; Lin, Y.-S.; Haynes, C. L. *ACS Nano* **2010**, *4*, 3363–3373.
(20) He, Q.; Zhang, Z.; Gao, Y.; Shi, J.; Li, Y. *Small* **2009**, *5*, 2722–2729.
(21) Thomassen, L. C. J.; Aerts, A.; Rabolli, V.; Lison, D.; Gonzalez, L.; Kirsch-Volders, M.; Napierska, D.; Hoet, P. H.; Kirschhock, C. E. A.; Martens, J. A. *Langmuir* **2009**, *26*, 328–335.
(22) Slowing, I. I.; Wu, C.-W.; Vivero-Escoto, J. L.; Lin, V. S. Y. *Small* **2009**, *5*, 57–62.
(23) Yu, T.; Malugin, A.; Ghandehari, H. *ACS Nano* **2011**, *5*, 5717–5728.
(24) Morishige, T.; Yoshioka, Y.; Inakura, H.; Tanabe, A.; Yao, X.; Narimatsu, S.; Monobe, Y.; Imazawa, T.; Tsunoda, S.-i.; Tsutsumi, Y.; Mukai, Y.; Okada, N.; Nakagawa, S. *Biomaterials* **2010**, *31*, 6833–6842.
(25) Brinker, C. J.; Kirkpatrick, R. J.; Tallant, D. R.; Bunker, B. C.; Montez, B. *J. Non-Cryst. Solids* **1988**, *99*, 418–428.

(26) Fadeel, B.; Garcia-Bennett, A. E. *Adv. Drug Delivery Rev.* **2010**, *62*, 362−374.
(27) Nel, A. E.; Madler, L.; Velegol, D.; Xia, T.; Hoek, E. M. V.; Somasundaran, P.; Klaessig, F.; Castranova, V.; Thompson, M. *Nat. Mater.* **2009**, *8*, 543−557.
(28) Nash, T.; Allison, A. C.; Harington, J. S. *Nature* **1966**, *210*, 259−261.
(29) Zhuravlev, L. T. *Langmuir* **1987**, *3*, 316−318.
(30) Stöber, W.; Fink, A.; Bohn, E. *J. Colloid Interface Sci.* **1968**, *26*, 62−69.
(31) Fenoglio, I.; Prandi, L.; Tomatis, M.; Fubini, B. *Redox Report* **2001**, *6*, 235−241.
(32) Fubini, B.; Mollo, L.; Giamello, E. *Free Radical Research* **1995**, *23*, 593−614.
(33) Gallas, J. P.; Lavalley, J. C.; Burneau, A.; Barres, O. *Langmuir* **1991**, *7*, 1235−1240.
(34) George, S.; Pokhrel, S.; Xia, T.; Gilbert, B.; Ji, Z.; Schowalter, M.; Rosenauer, A.; Damoiseaux, R.; Bradley, K. A.; Mädler, L.; Nel, A. E. *ACS Nano* **2009**, *4*, 15−29.
(35) Zhang, H.; Ji, Z.; Xia, T.; Meng, H.; Low-Kam, C.; Liu, R.; Pokhrel, S.; Lin, S.; Wang, X.; Liao, Y. P.; Wang, M.; Li, L.; Rallo, R.; Damoiseaux, R.; Telesca, D.; Madler, L.; Cohen, Y.; Zink, J. I.; Nel, A. E. *ACS Nano* **2012**, *6*, 4349−4368.
(36) Birmingham, A.; Selfors, L. M.; Forster, T.; Wrobel, D.; Kennedy, C. J.; Shanks, E.; Santoyo-Lopez, J.; Dunican, D. J.; Long, A.; Kelleher, D.; Smith, Q.; Beijersbergen, R. L.; Ghazal, P.; Shamu, C. E. *Nat Meth* **2009**, *6*, 569−575.
(37) Zhang, X. D. *Journal of Biomolecular Screening* **2007**, *12*, 645−655.
(38) Zhang, X. D. *Genomics* **2007**, *89*, 552−561.
(39) Wang, X.; Xia, T.; Duch, M. C.; Ji, Z.; Zhang, H.; Li, R.; Sun, B.; Lin, S.; Meng, H.; Liao, Y. P.; Wang, M.; Song, T. B.; Yang, Y.; Hersam, M. C.; Nel, A. E. *Nano Lett* **2012**, *12*, 3050−3061.
(40) Hamilton, R.; Wu, N.; Porter, D. W.; Buford, M.; Wolfarth, M.; Holian, A. *Particle and Fibre Toxicology* **2009**, *6*, 35.
(41) Martin, J. E.; Hurd, A. J. *Journal of applied Crystallography* **1987**, *20*, 61−78.
(42) Martin, J. E.; Schaefer, D. W.; Hurd, A. J. *Phys. Rev. A* **1986**, *33*, 3540−3543.
(43) Schaefer, D. W.; Olivier, B. J.; Hurd, A. J.; Beaucage, G. B.; Ivie, J. J.; Herd, C. R. *J. Aerosol Sci.* **1991**, *22* (Supplement 1), S447−S450.
(44) Schaefer, D. W.; Keefer, K. D. In *Fractals in Physics*; Pietronero, L., Tosatt, E., Eds.; North Holland: Amsterdam, 1986, p 39−45.
(45) Vaccaro, G.; Agnello, S.; Buscarino, G.; Gelardi, F. M. *J. Phys. Chem. C* **2010**, *114*, 13991−13997.
(46) Fan, H. Y.; Hartshorn, C.; Buchheit, T.; Tallant, D.; Assink, R.; Simpson, R.; Kisse, D. J.; Lacks, D. J.; Torquato, S.; Brinker, C. J. *Nat. Mater.* **2007**, *6*, 418−423.
(47) Armistead, C. G.; Tyler, A. J.; Hambleton, F. H.; Mitchell, S. A.; Hockey, J. A. *The Journal of Physical Chemistry* **1969**, *73*, 3947−3953.
(48) Mueller, R.; Kammler, H. K.; Wegner, K.; Pratsinis, S. E. *Langmuir* **2002**, *19*, 160−165.
(49) Gallas, J.-P.; Goupil, J.-M.; Vimont, A.; Lavalley, J.-C.; Gil, B.; Gilson, J.-P.; Miserque, O. *Langmuir* **2009**, *25*, 5825−5834.
(50) Taylor, J. A. G.; Hockey, J. A. *The Journal of Physical Chemistry* **1966**, *70*, 2169−2172.
(51) Fubini, B.; Fenoglio, I.; Ceschino, R.; Ghiazza, M.; Martra, G.; Tomatis, M.; Borm, P.; Schins, R.; Bruch, J. *International Journal of Hygiene and Environmental Health* **2004**, *207*, 89−104.
(52) Goller, D. D.; Phillips, R. T.; Sayce, I. G. *J. Non-Cryst. Solids* **2009**, *355*, 1747−1754.
(53) Warren, W. L.; Lenahan, P. M.; Jeffrey Brinker, C. *J. Non-Cryst. Solids* **1991**, *136*, 151−162.
(54) Vallyathan, V.; Shi, X.; Castranova, V. *Environmental health perspectives* **1998**, *106* (Suppl5), 1151−1155.
(55) Narayanasamy, J.; Kubicki, J. D. *J. Phys. Chem. B* **2005**, *109*, 21796−21807.
(56) Vallyathan, V. *Environ Health Perspect* **1994**, *102*, 111−115.
(57) Donaldson, K.; Borm, P. J. A. *Ann. Occup. Hyg.* **1998**, *42*, 287−294.
(58) Cassel, S. L.; Eisenbarth, S. C.; Iyer, S. S.; Sadler, J. J.; Colegio, O. R.; Tephly, L. A.; Carter, A. B.; Rothman, P. B.; Flavell, R. A.; Sutterwala, F. S. *Proceedings of the National Academy of Sciences* **2008**, *105*, 9035−9040.
(59) Dostert, C.; Pétrilli, V.; Van Bruggen, R.; Steele, C.; Mossman, B. T.; Tschopp, J. *Science* **2008**, *320*, 674−677.
(60) Ji, Z.; Wang, X.; Zhang, H.; Lin, S.; Meng, H.; Sun, B.; George, S.; Xia, T.; Nel, A. E.; Zink, J. I. *ACS Nano* **2012**, *6*, 5366−5380.
(61) Griscom, D. L.; Brinker, C. J.; Ashley, C. S. *J. Non-Cryst. Solids* **1987**, *92*, 295−301.
(62) Brinker, C. J.; Bunker, B. C.; Tallant, D. R.; Ward, K. J. *Journal de Chimie Physique et de Physico-Chimie Biologique* **1986**, *83*, 851−858.
(63) Napierska, D.; Thomassen, L. C. J.; Rabolli, V.; Lison, D.; Gonzalez, L.; Kirsch-Volders, M.; Martens, J. A.; Hoet, P. H. *Small* **2009**, *5*, 846−853.
(64) Diociaiuti, M.; Bordi, F.; Gataleta, L.; Baldo, G.; Crateri, P.; Paoletti, L. *Environmental Research* **1999**, *80*, 197−207.
(65) Razzaboni, B. L.; Bolsaitis, P. *Environ Health Perspect* **1990**, *87*, 337−341.
(66) Gerashchenko, B. I.; Gun'ko, V. M.; Gerashchenko, I. I.; Mironyuk, I. F.; Leboda, R.; Hosoya, H. *Cytometry* **2002**, *49*, 56−61.
(67) Murashov, V.; Harper, M.; Demchuk, E. *Journal of Occupational Hygiene* **2006**, *3*, 718−723.
(68) Lee, J.; Lee, Y.; Youn, J. K.; Na, H. B.; Yu, T.; Kim, H.; Lee, S.-M.; Koo, Y.-M.; Kwak, J. H.; Park, H. G.; Chang, H. N.; Hwang, M.; Park, J.-G.; Kim, J.; Hyeon, T. *Small* **2008**, *4*, 143−152.
(69) Marar, T. *Chemico-Biological Interactions* **2011**, *193*, 149−153.
(70) Sato, Y.; Kamo, S.; Takahashi, T.; Suzuki, Y. *Biochemistry* **1995**, *34*, 8940−8949.
(71) Meng, H.; Yang, S.; Li, Z.; Xia, T.; Chen, J.; Ji, Z.; Zhang, H.; Wang, X.; Lin, S.; Huang, C.; Zhou, Z. H.; Zink, J. I.; Nel, A. E. *ACS Nano* **2011**, *5*, 4434−4447.
(72) Zhao, Y.; Sun, X.; Zhang, G.; Trewyn, B. G.; Slowing, I. I.; Lin, V. S. Y. *ACS Nano* **2011**, *5*, 1366−1375.
(73) Tschopp, J.; Schroder, K. *Nat Rev Immunol* **2010**, *10*, 210−215.
(74) Ashley, C. E.; Carnes, E. C.; Phillips, G. K.; Padilla, D.; Durfee, P. N.; Brown, P. A.; Hanna, T. N.; Liu, J.; Phillips, B.; Carter, M. B.; Carroll, N. J.; Jiang, X.; Dunphy, D. R.; Willman, C. L.; Petsev, D. N.; Evans, D. G.; Parikh, A. N.; Chackerian, B.; Wharton, W.; Peabody, D. S.; Brinker, C. J. *Nat. Mater.* **2011**, *10*, 389−397.